

Structures of the magnetoionic media around the FR I radio galaxies 3C 31 and Hydra A

R.A. Laing ^{*1}, A.H. Bridle ², P. Parma ³, M. Murgia ^{3,4}

¹ *European Southern Observatory, Karl-Schwarzschild-Straße 2, D-85748 Garching-bei-München, Germany*

² *National Radio Astronomy Observatory, Edgemont Road, Charlottesville, VA 22903-2475, U.S.A.*

³ *INAF – Istituto di Radioastronomia, via Gobetti 101, I-40129 Bologna, Italy*

⁴ *INAF - Osservatorio Astronomico di Cagliari, Loc. Poggio dei Pini, Strada 54, I-09012 Capoterra (CA), Italy*

Received

ABSTRACT

We use high-quality Very Large Array (VLA) images of the Fanaroff & Riley Class I radio galaxy 3C 31 at six frequencies in the range 1365 to 8440 MHz to explore the spatial scale and origin of the rotation measure (RM) fluctuations on the line of sight to the radio source. We analyse the distribution of the degree of polarization to show that the large depolarization asymmetry between the North and South sides of the source seen in earlier work largely disappears as the resolution is increased. We show that the depolarization seen at low resolution results primarily from unresolved gradients in a Faraday screen in front of the synchrotron-emitting plasma. We establish that the residual degree of polarization in the short-wavelength limit should follow a Burn law and we fit such a law to our data to estimate the residual depolarization at high resolution. We discuss how to interpret the structure function of RM fluctuations in the presence of a finite observing beam and how to address the effects of incomplete sampling of RM distribution using a Monte Carlo approach. We infer that the observed RM variations over selected areas of 3C 31, and the small residual depolarization found at high resolution, are consistent with a power spectrum of magnetic fluctuations in front of 3C 31 whose power-law slope changes significantly on the scales sampled by our data. The power spectrum $P(f)$ can only have the form expected for Kolmogorov turbulence [$P(f) \propto f^{-11/3}$] on scales $\lesssim 5$ kpc. On larger scales we find $P(f) \propto f^{-2.3}$. We briefly discuss the physical interpretation of these results. We also compare the global variations of RM across 3C 31 with the results of three-dimensional simulations of the magnetic-field fluctuations in the surrounding magnetoionic medium. We infer that the RM variation across 3C 31 is qualitatively as expected from relativistic-jet models of the brightness asymmetry wherein the apparently brighter jet is on the near side of the nucleus and is seen through less magnetoionic material than the fainter jet. We show that our data are inconsistent with observing 3C 31 through a spherically-symmetric magnetoionic medium, but that they are consistent with a field distribution that favors the plane perpendicular to the jet axis – probably because the radio source has evacuated a large cavity in the surrounding medium. We also apply our analysis techniques to the case of Hydra A, where the shape and the size of the cavities produced by the source in the surrounding medium are known from X-ray data. We emphasise that it is essential to account for the potential exclusion of magnetoionic material from a large volume containing the radio source when using the RM variations to derive statistical properties of the fluctuations in the foreground magnetic field.

Key words: galaxies: jets – radio continuum:galaxies – magnetic fields – polarization – galaxies:ISM – X-rays: galaxies

1 INTRODUCTION

The hot intracluster medium in rich clusters of galaxies is magnetised, with field strengths which are important

* E-mail: rlaing@eso.org

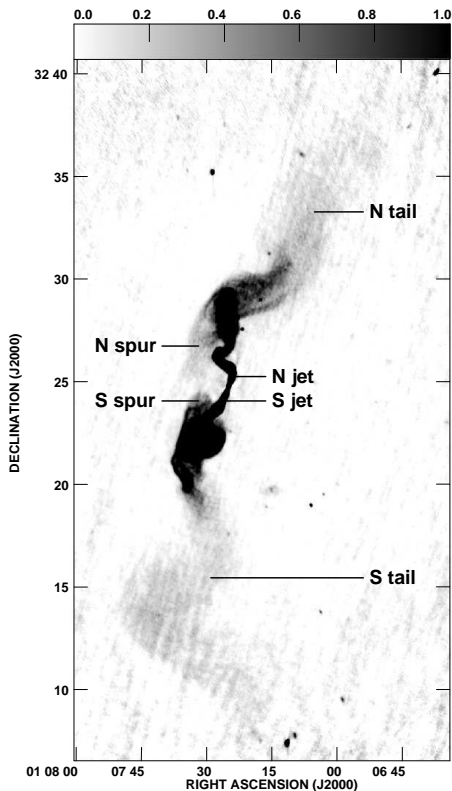


Figure 1. Grey scale at 5.5 arcsec FWHM resolution showing the main regions of 3C 31 in total intensity at 1.4 GHz as defined by Laing et al. (2008, fig. 1b). This image shows the radio source in equatorial co-ordinates, while the displays of depolarization and rotation measure below have been rotated anti-clockwise by 19.7 deg to make the inner jet axis vertical.

for the suppression of heat conduction, even if not dynamically significant (Carilli & Taylor 2002, and references therein). The fields are apparent via synchrotron radiation from cluster halo sources and Faraday rotation of polarized emission from embedded and background sources (the subject of the present paper). At high spatial resolution, the rotation of the \mathbf{E} -vector position angle is accurately proportional to the square of the wavelength and depolarization with increasing wavelength is small, indicating that a foreground medium is responsible. Imaging of these foreground Faraday rotation measure (RM) variations across radio sources in clusters has recently been used to estimate the power spectrum of RM and, by implication, of magnetic-field fluctuations, in turn leading to improved estimates of field strength (Enßlin & Vogt 2003; Vogt & Enßlin 2003, 2005; Murgia et al. 2004; Govoni et al. 2006; Guidetti et al. 2008). RM fluctuations are also seen against radio sources in sparser environments such as galaxy groups (e.g. Perley, Bridle & Willis 1984; Laing & Bridle 1987), but the structure and strength of the magnetic fields in these systems have not been studied in detail.

RM variations in clusters of galaxies have normally been modelled assuming that the magnetic field is tangled either on a single scale (Burn 1966; Felten 1996) or over a range of scales (e.g. Enßlin & Vogt 2003; Murgia et al. 2004) and embedded in a smoothly varying, spherically symmetric den-

sity distribution with parameters derived from X-ray observations. This interpretation is complicated by three effects:

(i) It is usually impossible to locate a radio galaxy along the line of sight within a cluster, and the path length over which Faraday rotation occurs is therefore not well determined. It often has to be assumed that the sources are in the cluster mid-plane.

(ii) The sources are inclined to the line of sight and may be extended on scales comparable with changes in external density, so the Faraday depth will vary systematically over the radio structure. The observed correlation between depolarization and jet sidedness (in the sense that the side of the source containing the brighter jet depolarizes less rapidly with increasing wavelength) is most easily interpreted in this way: if the nearer jet is brighter as a result of Doppler boosting, then its emission is seen through less magnetoionic material and therefore suffers less Faraday rotation (Laing 1988). Although the general association between depolarization asymmetry and jet sidedness is well documented in both weak and powerful sources (Morganti et al. 1997; Garrington & Conway 1991), there are as yet few sources that exhibit asymmetric depolarization for which it has been clearly established that the Faraday rotation is indeed due to a foreground medium (although there are no known counter-examples). The best-observed examples are all in central cluster galaxies with cooling cores: Cygnus A (Dreher, Carilli & Perley 1987); M 87 (Owen, Eilek & Keel 1990); Hydra A (Taylor & Perley 1993) and Hercules A (Gizani & Leahy 1999).

(iii) Radio sources must interact with their environments, leading to local deviations from spherical symmetry in the density distribution. There is direct evidence for the presence of evacuated cavities in the hot plasma coincident with the radio lobes of sources in clusters, as predicted by models of radio-source evolution (Scheuer 1974; McNamara & Nulsen 2007). Magnetic fields in the surrounding medium may be important in stabilizing the cavities against Kelvin-Helmholtz and Rayleigh-Taylor instabilities (Dursi & Pfrommer 2008).

In the present paper, we image and model the Faraday rotation distribution across the bright FRI (Fanaroff & Riley 1974) class radio source 3C 31. This source is identified with the nearby elliptical galaxy NGC 383, which is the brightest member of a rich group of galaxies (Arp 1966; Zwicky & Kowal 1968). We therefore probe a different environment from the Abell clusters studied by previous authors. Hot gas associated with the galaxy has been detected on both the group and galactic scales by X-ray imaging (Komossa & Böhringer 1999; Hardcastle et al. 2002). The nucleus of the source is located at the centre of the hot gas distribution, simplifying the geometry, and the orientation is well constrained, at least for the inner jets (Laing & Bridle 2002a). 3C 31 shows a pronounced depolarization asymmetry in the expected sense (Burch 1979; Strom et al. 1983; Andernach et al. 1992). Because it is bright, highly polarized, and well resolved in both dimensions (Laing et al. 2008, and references therein), the variation of the Faraday rotation measure across it can be studied in unusually rich detail. We can make a stringent test of the hypothesis of foreground rotation and evaluate the spatial statistics of RM over different parts of the source.

As the jet orientation is well constrained, we have a unique opportunity to compare the global changes in RM fluctuation amplitude across the structure with the predictions of three-dimensional models, including the effects of departures from spherical symmetry. 3C 31 therefore provides an opportunity to examine the kiloparsec-scale structure of the magnetoionic medium in an environment that may be more characteristic of the FRI population as a whole than the clusters which have been the subject of many earlier studies.

We will show that our three-dimensional analysis of 3C 31 is most consistent with the hypothesis that the radio source has evacuated large cavities which are essentially devoid of thermal plasma, although existing X-ray observations of the NGC 383 group are not deep enough to image such cavities if they are present. This motivated us to apply our techniques to the RM distribution of a second source, Hydra A, in which the cavities are well characterised (Wise et al. 2007).

Section 2 of the present paper presents the main features of our data on the distributions of the Faraday rotation and depolarization of the polarized emission from 3C 31, and Section 3 gives an overview of our analysis and general assumptions. Sections 4 and 5 discuss the structure of the magnetic field in the foreground screen that is responsible for the Faraday rotation measure fluctuations. Section 4 describes our analysis of the two-dimensional spatial statistics of the RM fluctuations. Section 5 explores three-dimensional models of the magnetoionic medium consistent with this two-dimensional analysis. Section 6 presents an analysis of the RM distribution in Hydra A. Section 7 summarises our conclusions. Some mathematical details are given in Appendices A and B and an analysis of the effects of partially-foreverground rotation is described in Appendix C.

Throughout this paper, we take NGC 383 to have a redshift of 0.0169 (the mean value from Smith et al. 2000, Huchra, Vogeley & Geller 1999 and De Vaucouleurs et al. 1991). We assume a concordance cosmology with a Hubble Constant $H_0 = 70 \text{ km s}^{-1} \text{ Mpc}^{-1}$, $\Omega_\Lambda = 0.7$ and $\Omega_M = 0.3$. At the redshift of NGC 383, this gives a linear scale of $0.344 \text{ kpc arcsec}^{-1}$. For Hydra A, we take $z = 0.0549$ (Smith et al. 2004) and a linear scale of $1.067 \text{ kpc arcsec}^{-1}$.

2 THE OBSERVED DEPOLARIZATION AND FARADAY ROTATION IN 3C 31

The observations and their reduction have been presented by Laing et al. (2008), along with discussions of spatial variations in the radio spectrum and salient features of the total intensity and the apparent magnetic-field structure – all intrinsic to the source. The principal large-scale features of the source discussed in that paper are shown schematically in Fig. 1. The data were obtained under NRAO observing proposals AF236 and AL405 at six frequencies - 1365, 1435, 1485, 1636, 4985 and 8440 MHz - with angular resolutions of 1.5 and 5.5 arcsec. The high quality and good sampling of the λ^2 and angular domains in these data make them well suited for analysis of the statistics of the Faraday rotation and depolarization across 3C 31.

Magnetised thermal plasma along the line of sight causes Faraday rotation of the plane of polarization of lin-

early polarized radiation, quantified by the rotation measure, RM [equations (A1) – (A3)]. If the thermal plasma is mixed with the emitting material or if there are variations of foreground Faraday rotation across the beam, the emission tends to depolarize with increasing wavelength. We will show that all of our observations are consistent with the expected variation of polarization with wavelength for an almost completely resolved foreground screen. In Section 2.1, we establish some essential theoretical results which underpin this analysis. We discuss the observed depolarization, the evidence that the Faraday rotating medium associated with 3C 31 is entirely in front of the radio source, and the variations of RM across the structure in Sections 2.2, 2.3 and 2.4, respectively.

2.1 The effects of partial resolution for a foreground screen

The observing beam modifies the derived spatial statistics of RM. In practice, we derive \mathbf{E} -vector position angle from Q and U images convolved with the beam and use the position angles at multiple frequencies to calculate RM. The beam has the effect of suppressing high spatial frequencies but for wavelengths close to 0 (and consequently low depolarization), this effect can be evaluated simply. The argument, which is fundamental to the analysis in Section 4, is as follows (Tribble 1991a). For a complex polarization

$$\mathbf{p}(\lambda) = |\mathbf{p}(\lambda)| \exp[2i\chi(\lambda^2)]$$

defined to have zero position angle for $\lambda = 0$, the RM at any wavelength is given by

$$\begin{aligned} \text{RM} &= \frac{\partial \chi}{\partial \lambda^2} \\ &= \frac{1}{2} \Im \left(\frac{\partial \ln \mathbf{p}}{\partial \lambda^2} \right) \end{aligned}$$

In the case of pure foreground rotation, $|\mathbf{p}|$ is independent of λ . If, in addition, it does not vary over a beam $W(\mathbf{r}_\perp)$ of unit area, i.e. $\mathbf{p}(\mathbf{r}_\perp, \lambda) = \mathbf{p}_0$, where \mathbf{p}_0 is a constant and \mathbf{r}_\perp is a vector in the plane of the sky, then the measured polarization is

$$\overline{\mathbf{p}(\mathbf{r}_\perp, \lambda)} = |\mathbf{p}_0| \int W(\mathbf{r}_\perp - \mathbf{r}'_\perp) \exp[2i\text{RM}(\mathbf{r}'_\perp)\lambda^2] d^2\mathbf{r}'_\perp$$

The observed RM is derived by differentiating under the integral sign and taking the zero-wavelength limit:

$$\overline{\text{RM}(\mathbf{r}_\perp)} = \int W(\mathbf{r}_\perp - \mathbf{r}'_\perp) \text{RM}(\mathbf{r}'_\perp) d^2\mathbf{r}'_\perp \quad (1)$$

i.e. *the measured RM distribution is closely approximated by the convolution of the true RM distribution with the observing beam.* We use this result to include the observing beam explicitly in our analysis, verifying post hoc that the approximation is valid.

This approach also makes it easy to see why λ^2 rotation persists even in the presence of small but significant depolarization. Consider a circular Gaussian beam $W(\mathbf{r}_\perp) = \exp(-r_\perp^2/2\sigma^2)/2\pi\sigma^2$. To first order

$$\text{RM}(\mathbf{r}_\perp) \approx \text{RM}(\mathbf{0}) + \mathbf{r}_\perp \cdot \nabla \text{RM}$$

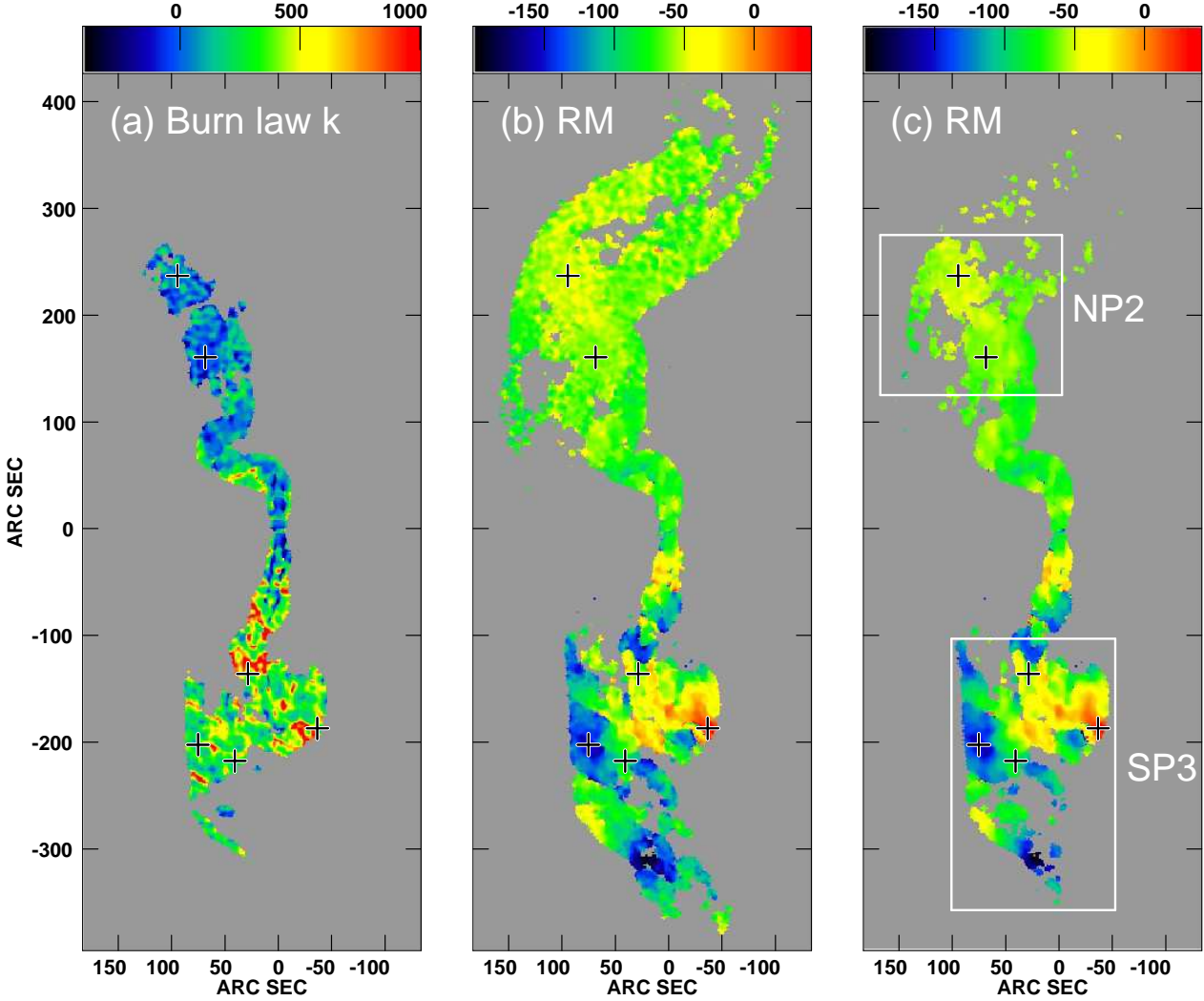


Figure 2. Depolarization and rotation measure at a resolution of 5.5 arcsec FWHM. (a) Burn law k in $\text{rad}^2 \text{m}^{-4}$, derived from a weighted least-squares fit to the relation $\ln[p(\lambda)] = \ln[p(0)] - k\lambda^4$ between 4985 and 1365 MHz. The colour range is from -400 to $1000 \text{ rad}^2 \text{m}^{-4}$. (b) RM from a fit to the four frequencies between 1636 and 1365 MHz, primarily to show the RM in the North tail and spur. The range is -200 to -33 rad m^{-2} . (c) as (b), but using 5 frequencies between 4985 and 1365 MHz. The errors are smaller than in panel (b), but fewer points in the North of the source have sufficient signal to determine the RM. The rectangles marked ‘NP2’ and ‘SP3’ denote the regions for the RM histograms in Fig. 8(a) and (e) and the structure-function analysis of Section 4.4. The crosses mark the positions for the plots in Figs 4 and 6.

where ∇RM is also evaluated at $\mathbf{r}_\perp = \mathbf{0}$. The integral for $\mathbf{p}(\lambda)$ can then be evaluated analytically to give:

$$\overline{\mathbf{p}(\lambda)} \approx |\mathbf{p}| \exp[2i(\text{RM}(\mathbf{0}) + \mathbf{r}_\perp \cdot \nabla \text{RM})\lambda^2] \times \exp[-2|\nabla \text{RM}|^2 \sigma^2 \lambda^4] \quad (2)$$

The first exponential term corresponds to λ^2 rotation and the second to depolarization. Thus if the RM varies by a small amount across the beam, then we expect λ^2 rotation even though there is significant (albeit small) depolarization. The wavelength dependence of depolarization has the functional form derived by Burn (1966):

$$p(\lambda) = p(0) \exp(-k\lambda^4) \quad (3)$$

with $k = 2|\nabla \text{RM}|^2 \sigma^2$, but note that this will not in general persist at longer wavelengths (Tribble 1991a, see Section 4.5 and Appendix C).

2.2 Depolarization

The effect of depolarization between two wavelengths λ_1 and λ_2 is usually expressed in terms of the ratio $\text{DP}_{\lambda_1}^{\lambda_2} = p(\lambda_2)/p(\lambda_1)$, where $p(\lambda)$ is the degree of polarization. Our six-frequency data set is capable of providing more sophisticated information about the depolarization, but to make effective use of it we need a suitable fitting function. As we have shown in Section 2.1, a Burn law variation [Burn 1966; equations (2) and (3)], is expected for partially resolved foreground Faraday rotation in the short-wavelength limit. The data at the vast majority of individual pixels are fit to within the errors by this relation and we show images of k at 5.5 and 1.5-arcsec resolution in Figs. 2(a) and 3(a).¹ Errors in

¹ The wavelength dependences at a small minority of points in the 5.5-arcsec images of the Southern part of the source show

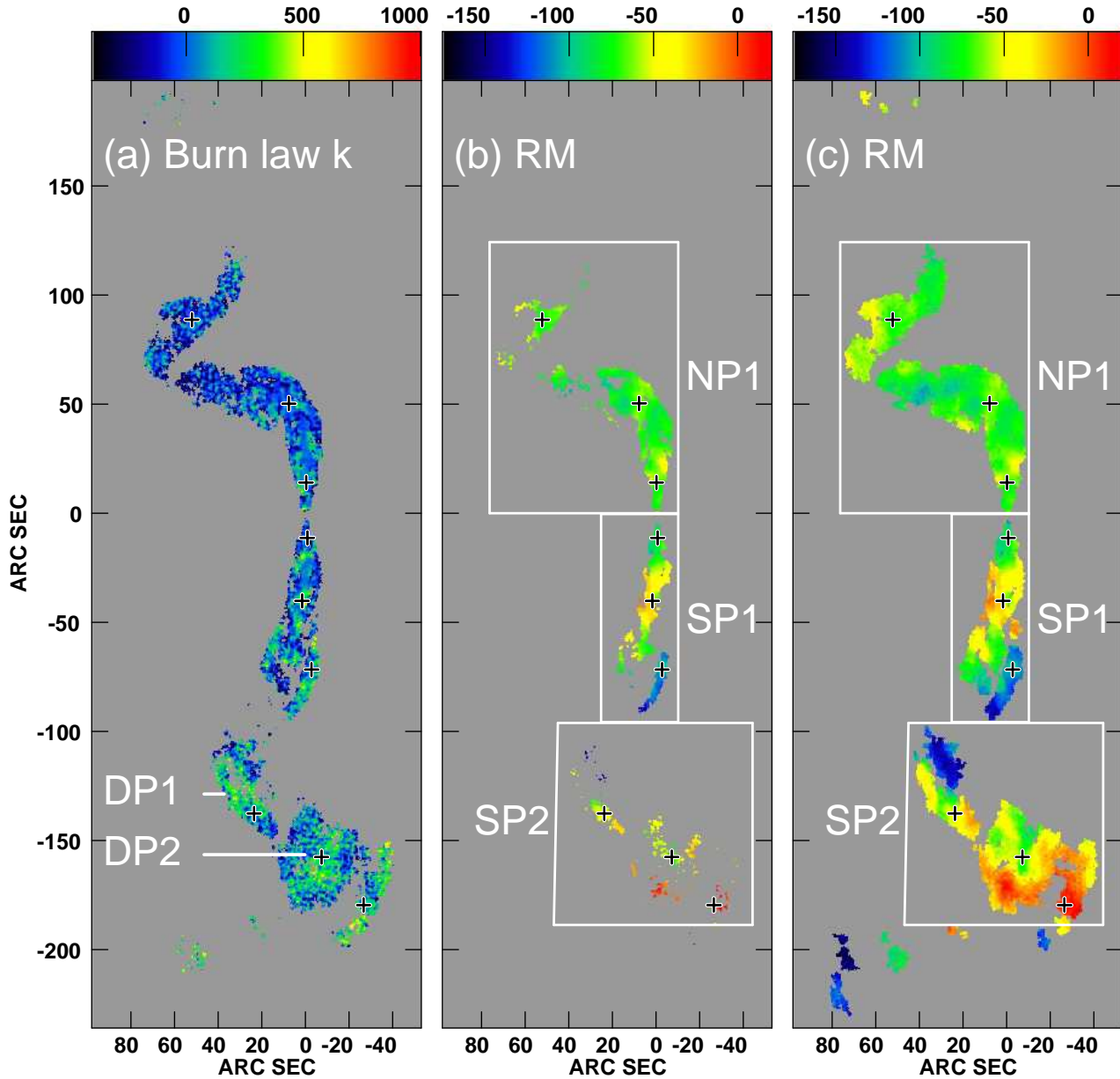


Figure 3. Depolarization and rotation measure at a resolution of 1.5 arcsec FWHM. (a) Burn law k in $\text{rad}^2 \text{m}^{-4}$, derived from a weighted least-squares fit to the relation $\ln[p(\lambda)] = \ln[p(0)] - k\lambda^4$ for six frequencies between 8440 and 1365 MHz. The colour range is from -400 to $1000 \text{ rad}^2 \text{m}^{-4}$, as in Fig. 2(a). (b) RM determined by a fit to position-angle images at 6 frequencies between 1365 and 8440 MHz using a version of the AIPS task RM modified by G.B. Taylor. The colour range is -180 to $+20 \text{ rad m}^{-2}$. The boxes NP1, SP1 and SP2 show the areas used for the RM histograms in Fig. 8 and for the structure-function analysis in Section 4.4. (c) As (b), but using the PACERMAN algorithm of Dolag, Vogt & Enßlin (2005). The crosses mark the positions for the plots in Figs 5 and 7.

k due to rotation across the observing bands are negligible for the bandwidths used for these observations (Laing et al. 2008, table 1) and the observed Faraday rotations (see Section 2.3).

The well-established depolarization asymmetry between the North and South sides of 3C 31 (Burch 1979; Strom et al. 1983) is still present at a resolution of 5.5 arcsec, although reduced in amplitude from that in the lower resolution

significant deviations from a Burn law. We return to this and related issues in Section 4.5 and Appendix C.

data. Fig. 2(a) shows k derived from a fit to 5-frequency data between 1365 and 4985 MHz at this resolution. Example plots of p against λ^4 are shown in Fig. 4 in order to demonstrate that the Burn law gives adequate fits for this frequency range and resolution. Significant depolarization ($k > 0$) is found at most individual points, but a minority have $k < 0$ due to noise or the effects of Faraday rotation on a non-uniform distribution of intrinsic polarization. The mean values for the North and South of the source are $\langle k \rangle = 83 \text{ rad}^2 \text{m}^{-4}$ and $\langle k \rangle = 364 \text{ rad}^2 \text{m}^{-4}$, respectively, corresponding to $\text{DP}_{6\text{cm}}^{22\text{cm}} \approx 0.8$ and 0.4 , compared with ~ 1

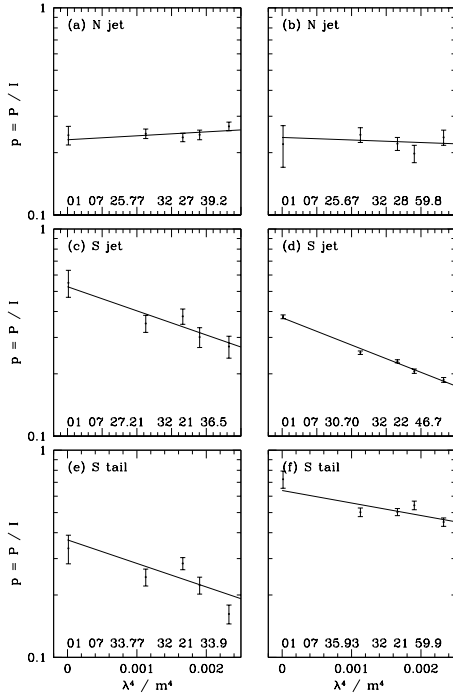


Figure 4. Plots of degree of polarization, p (log scale), against λ^4 at the positions indicated by crosses in Fig. 2 and quoted in the individual panels. The resolution is 5.5 arcsec FWHM. Burn law fits [equation (3)] are also plotted.

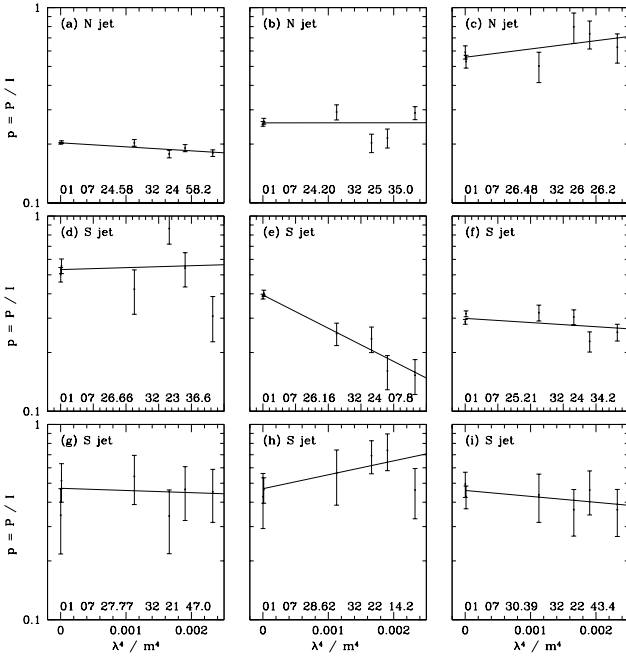


Figure 5. Plots of degree of polarization, p (log scale), against λ^4 at the positions indicated by crosses in Fig. 3 and quoted in the individual panels. The resolution is 1.5 arcsec. Burn law fits [equation (3)] are also plotted. Of the fits in this figure, only (a) and (e) show significant depolarization.

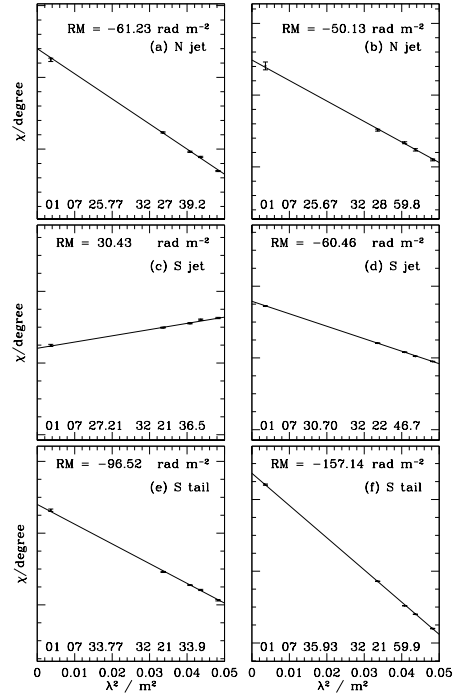


Figure 6. Plots of **E**-vector position angle χ against λ^2 at the positions indicated in Fig. 2. The resolution is 5.5 arcsec FWHM. Fits to $\chi(\lambda^2) = \chi(0) + \text{RM}\lambda^2$ are shown, and the values of RM are given in the individual panels. The ranges in angle are 300° in panels (a) – (b) and 600° elsewhere.

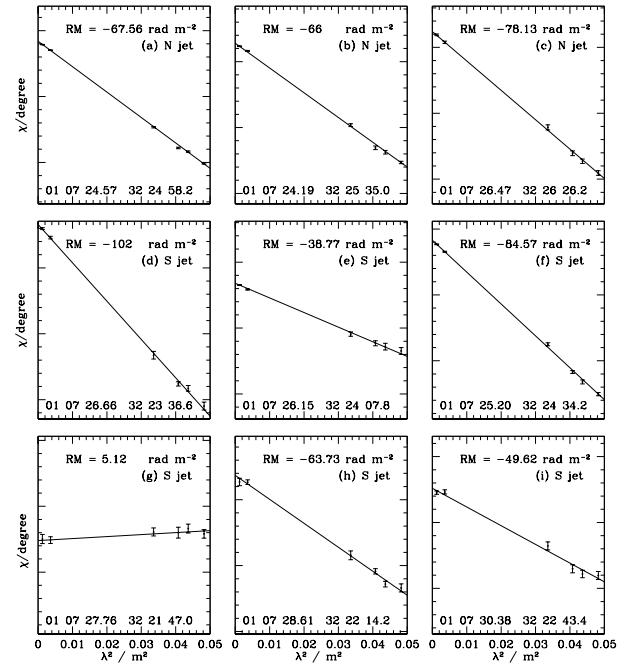


Figure 7. Plots of **E**-vector position angle χ against λ^2 at the positions indicated by crosses in Fig. 3. Fits to $\chi(\lambda^2) = \chi(0) + \text{RM}\lambda^2$ are shown, and the values of RM are given in the individual panels. The resolution is 1.5 arcsec FWHM and the position-angle range is 300° .

and 0.1 – 0.3 at resolution of $24 \text{ arcsec} \times 47 \text{ arcsec}$ FWHM (Strom et al. 1983).

Comparison between Figs 2(a) and 3(a) shows further that there is much less depolarization at 1.5-arcsec resolution. The data at this resolution are noisy and the fitted values of k are consistent with zero at the majority of individual points (many points therefore have $k < 0$). Of the sky positions shown in Fig. 5, only (a) and (e) show significant depolarization, for example. Positions with $k > 0$ tend to occur in coherent clumps (the two most prominent are labelled DP1 and DP2 in Fig. 3a), indicating that the residual depolarization in the South is still significant, however. Simulation of our image analysis and fitting procedures shows that the distribution of errors in k is position-dependent and significantly asymmetrical over much of the source at 1.5-arcsec resolution, leading to biases in spatial averages. For quantitative comparisons, we therefore use only data with $p > 4\sigma_p$ at all frequencies, in which case we estimate systematic offsets in the mean values to be negligible compared with the quoted random errors. Averages over these positions confirm not only the decrease in depolarization with increasing resolution, but also the persistence of a residual difference between the two jets. In a high signal-to-noise region within 60 arcsec of the nucleus in the North jet, we find $\langle k \rangle = 3 \pm 7 \text{ rad}^2 \text{ m}^{-4}$ compared with $32 \text{ rad}^2 \text{ m}^{-4}$ at 5.5 arcsec resolution. Similarly, for the inner 60 arcsec of the South jet we find $\langle k \rangle = 55 \pm 7 \text{ rad}^2 \text{ m}^{-4}$ (1.5 arcsec) and $166 \text{ rad}^2 \text{ m}^{-4}$ (5.5 arcsec).

Apart from the large-scale North-South asymmetry, there is no compelling evidence for any detailed correlation between depolarization and source structure (as might be expected if the effect occurred in a thin surface layer just in front of the emitting material).

2.3 Faraday rotation: images and evidence for foreground rotation

RM images at 5.5-arcsec resolution made using a version of the AIPS task RM modified by G.B. Taylor are shown in Fig. 2(b) for the 1365–1636 MHz data alone and in Fig. 2(c) for all five frequencies between 1365 and 4985 MHz. The former is noisier in the region of overlap, but covers a wider area: the two images are consistent with each other where they overlap. Example fits of \mathbf{E} -vector position angle χ against λ^2 are shown in Fig. 6.

There is a clear asymmetry in RM fluctuation amplitude, which is much greater in the South. In the outer North jet, spur and tail, the low depolarization (Fig. 2a) and λ^2 rotation together indicate mostly resolved foreground Faraday rotation. For the parts of the North tail and spur which show significant polarized signal at 1365 to 1636 MHz but which are not detected at 4985 MHz, the depolarization found at lower resolution between these frequencies is also negligible (Strom et al. 1983). Large-scale coherent RM variations ($\approx 10 \text{ rad m}^{-2}$ on scales from $\approx 10 \text{ arcsec}$ up to $\approx 1 \text{ arcmin}$) are observed in this part of the source [Figs 2(b) and (c)]. These are large enough to account for the depolarization of 0.3–0.4 observed between 1.4 and 0.6 GHz with a beam of $29 \times 55 \text{ arcsec}^2$ (Strom et al. 1983). In the South spur and tail, despite the large RM gradients and significant depolarization, the rotation remains accurately proportional to λ^2 except at a few positions. These are usually associated with

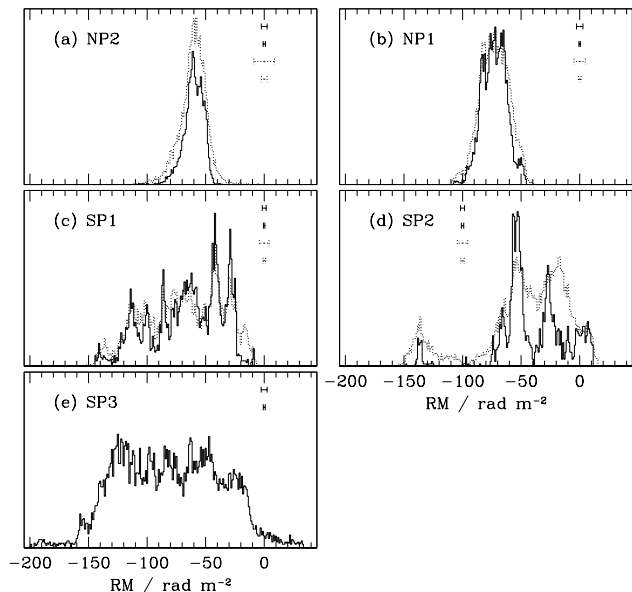


Figure 8. Histograms of the RM distributions within the regions marked NP2, SP3 (Fig. 2), NP1, SP1 and SP2 (Fig. 3). (a) NP2. The RM distributions from 5- and 4-frequency fits at 5.5 arcsec FWHM are shown by full and dotted lines, respectively. (b) – (d) NP1, SP1 and SP2. The distributions at 1.5 arcsec FWHM from the AIPS and PACERMAN fitting algorithms are shown by the full and dotted lines, respectively. (e) SP3, showing the RM distribution from a 5-frequency fit at 5.5 arcsec FWHM. The histograms have been scaled independently to approximately the same maximum value and the horizontal error bars show the mean and maximum rms errors derived from the RM fits.

abrupt changes in RM on scales comparable with the observing beam and high depolarization. We show in Appendix C that these effects are quantitatively consistent with Faraday rotation by a partially resolved foreground screen.

Images of rotation measure in the jets at 1.5-arcsec resolution using all 6 frequencies are shown in Fig. 3. We used two different fitting programs: the modified RM task [Fig. 3(b)] and the PACERMAN algorithm of Dolag et al. (2005, Fig. 3c). In the former case, we required that all \mathbf{E} -vector position angles at a given point had rms error $< 10^\circ$, but still found that a few points had wildly discrepant RM values due to erroneous resolution of $n\pi$ ambiguities. Unlike the effect noted at 5.5-arcsec resolution (where the RM anomalies are extended over several beamwidths), the errant values occurred at isolated pixels and cannot represent real RM structure. They were therefore edited out. The PACERMAN algorithm solves for the $n\pi$ ambiguities in regions of high signal-to-noise ratio and uses this information to resolve them in adjoining, fainter areas. Where RM solutions were found by both algorithms, they were in excellent agreement, but PACERMAN gave credible results for many more points with low signal-to-noise ratio, especially in the South.

At 1.5-arcsec resolution, there are no significant deviations from the relation $\Delta\chi \propto \lambda^2$ over a range of rotation $\Delta\chi$ up to $\sim 300^\circ$ (fits at representative points are shown in Fig. 7). Taken with the observation that the depolarization is very slight over our frequency range even in the South (Section 2.2), this implies that most, if not all of the Faraday rotation of the jet emission must be produced by

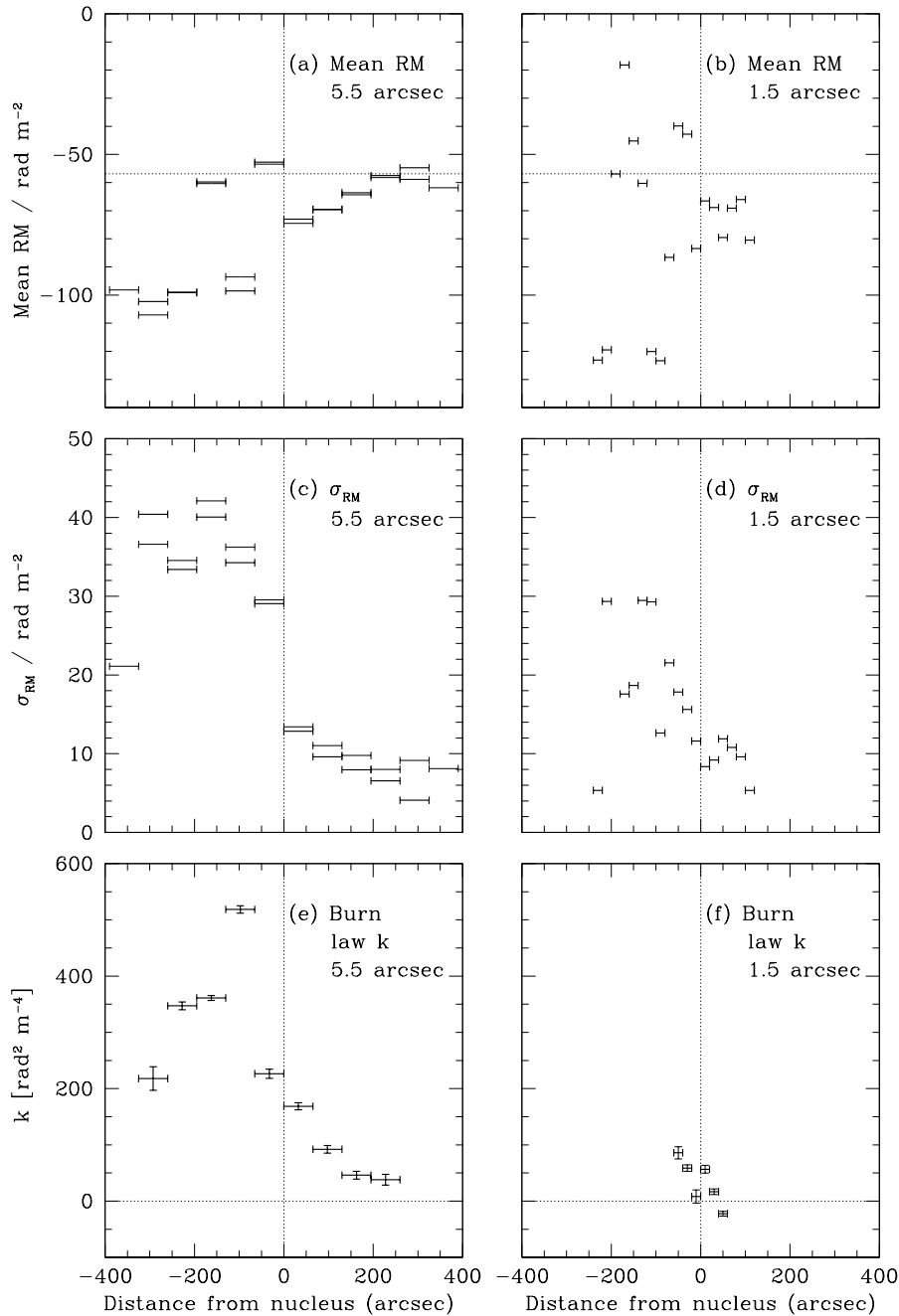


Figure 9. Profiles along an axis defined by the inner jets in 3C 31 (PA 19.7°). Positive distances are in the direction of the North jet and the vertical dotted lines show the position of the nucleus. Quantities are evaluated for boxes of length 65 arcsec along the axis for the 5.5 arcsec FWHM data (panels a, c and e) and 20 arcsec for the 1.5 arcsec FWHM data (panels b, d, f), using the PACERMAN fitting algorithm for the RM in the latter case. The boxes are wide enough to include all unblanked points. (a) and (b) Mean RM, $\langle \text{RM} \rangle$. The horizontal dotted line shows our adopted value of the foreground rotation measure, RM_0 . (c) and (d) σ_{RM} , determined with respect to the local mean in the box. The values of σ_{RM} have been corrected to first order for the offset due to noise on the fit. (e) and (f) Mean value of the Burn law parameter k , with statistical uncertainties estimated from the least-squares fits. Positive values imply depolarization with increasing wavelength and $k = 100 \text{ rad}^2 \text{ m}^{-4}$ corresponds to a depolarization ratio of 0.79 at 1365 MHz.

foreground material and that most of the depolarization observed at lower resolutions results from RM fluctuations on scales larger than 1.5 arcsec. The residual depolarization at 1.5 arcsec resolution is probably caused by RM fluctuations on even smaller scales. We cannot establish this conclusively without higher-resolution data, but we show consistency of

the observed wavelength dependence and magnitude of the depolarization with models of the spatial variation of foreground RM in Sections 2.1 and 4.5, respectively. The most extreme depolarization (e.g. regions DP1 and DP2) tend to be associated with large RM gradients, as expected for foreground models [Figs 3(a) and (c)].

2.4 Variation of Faraday rotation and depolarization along the jets

The RM distributions for regions NP1, NP2, SP1, SP2 and SP3 are plotted as histograms in Fig. 8. The results for 4- and 5-frequency fits are in good agreement for region NP2 [Fig. 8(a)], although the former are inevitably noisier. The AIPS and PACERMAN algorithms give very similar results for NP1 and SP1 but they disagree significantly in SP2, where the former fits many fewer points [Fig. 8(d)]. We use the 1.5-arcsec PACERMAN images and the 5.5-arcsec, 5-frequency fits for quantitative analysis. Note that the fitting errors (indicated by the error bars in Fig. 8) are generally much smaller than the widths of the histograms.

In the North, the RM distributions are sharply peaked with a total range from -100 to -40 rad m^{-2} . The inner N jet shows a similar range. In the South, the RM range is much larger (-200 to $+30 \text{ rad m}^{-2}$), and the distributions appear more uniform.

Fig. 9 shows profiles of the mean rotation measure, $\langle RM \rangle$, the rms with respect to this local mean, σ_{RM} and the parameter k in the Burn depolarization law along the inner jet axis (position angle 19.7 deg). The 5.5- and 1.5-arcsec data were averaged over boxes wide enough to contain all unblanked pixels and of lengths 65 and 20 arcsec along the axis, respectively. In order to avoid systematic errors, only points with $p > 4\sigma_p$ were used to generate the profiles of k . We made a first-order correction to the rms RM, σ_{RMraw} , by subtracting the fitting error σ_{fit} in quadrature to give $\sigma_{\text{RM}} = (\sigma_{\text{RMraw}}^2 - \sigma_{\text{fit}}^2)^{1/2}$, but the effect of this correction is in any case very small.

There is a systematic gradient in $\langle RM \rangle$ along the North jet, but the values vary erratically in the South. σ_{RM} increases from North to South from a minimum of $\approx 5 \text{ rad m}^{-2}$ at 5.5 arcsec resolution (300 arcsec North of the nucleus) to a maximum of $30\text{--}40 \text{ rad m}^{-2}$ (depending on resolution) at 200 arcsec to the South. There is only evidence for a decrease in the last box 400 arcsec from the nucleus in the South, where our data are limited in signal-to-noise and restricted to four observing frequencies. The profile of $\langle k \rangle$ at 5.5-arcsec resolution [Fig. 9(e)] shows that depolarization also increases monotonically from North to South across the nucleus, but there is evidence for a decrease in the South at larger distances. At 1.5 arcsec resolution, depolarization is significant only in the South jet. The differences between the two resolutions are as expected for partially resolved RM fluctuations: at higher resolution there is less depolarization and lower rms but variations between box means are larger. The increase in RM fluctuation amplitude going from North to South across the nucleus is striking.

The very small variation in $\langle RM \rangle$ in the North of the source suggests a Galactic origin. Estimates of the Galactic foreground RM derived from observations of nearby sources range from -64 to -39 rad m^{-2} (Andernach et al. 1992) and the value predicted by the smoothed models of Dineen & Coles (2005) is -49.3 rad m^{-2} , both consistent with this idea. The best estimate of the foreground RM from our own data comes from the region more than 200 arcsec North of the nucleus of 3C 31, where fluctuations are smallest [Fig. 9(a)]. In what follows, we adopt the unweighted mean RM from the 5-frequency fits over this region, $\text{RM}_0 = -56.9 \text{ rad m}^{-2}$, as the Galactic contribution.

Note, however, that we cannot exclude a significant large-scale component of RM local to this part of the source (Section 4.4).

2.5 Limits on internal Faraday rotation

Our limits on depolarization and deviations from λ^2 rotation, within 60 arcsec of the nucleus in the North jet can potentially constrain the internal density of thermal electrons. For a line of sight intersecting the jet axis 28 arcsec from the nucleus in projection (the maximum extent of the conservation-law model of Laing & Bridle 2002b), our kinematic model gives a path length through the jet of 7.3 kpc and an on-axis equipartition magnetic field of 1.5 nT (Laing & Bridle 2002a). We adopt these as fiducial numbers, noting that there will be variations in path length and field along and transverse to the jet axis and that the component of the magnetic field along the line of sight will be reduced due to projection.

We use the formulae given by Burn (1966), taking a conservative upper limit of $\langle k \rangle < 20 \text{ rad}^2 \text{ m}^{-4}$ (equivalent to a depolarization of > 0.95 at our lowest observing frequency of 1365 MHz). For a uniform magnetic field B along the line of sight and a path length L , this corresponds to a limit on the internal density of

$$n/\text{m}^{-3} \lesssim 120(B/1.5\text{nT})^{-1}(L/7.3\text{kpc})^{-1} \quad (4)$$

The lack of deviation from a λ^2 law requires that no more than $\approx 45^\circ$ of the total rotation is due to thermal matter distributed uniformly within the jet, giving $n \lesssim 370 \text{ m}^{-3}$ for the fiducial parameters and a uniform field. If, on the other hand, we assume that the field component along the line of sight has a Gaussian distribution with rms B and N reversals through the jet, we find

$$n/\text{m}^{-3} \lesssim 40(B/1.5\text{nT})^{-1}(L/7.3\text{kpc})^{-1}N^{1/2} \quad (5)$$

Our modelling of the magnetic-field structure in the jets (Laing & Bridle 2002a) implies that the magnetic field is dominated by the toroidal component, with a smaller longitudinal contribution. There are two extreme possibilities (Laing, Bridle & Canvin 2006):

- (i) The dominant toroidal component is vector-ordered, but the longitudinal component has many reversals. We would then expect systematic variations in Faraday rotation transverse to the jet axis, which we do not observe.
- (ii) The field is entirely disordered, but anisotropic.

In either model, there would be systematic (and so far unobserved) variations of depolarization across the jets, together with a gradient in RM if the toroidal component is ordered. A pure toroidal field has no component along the line of sight on the projected jet axis, so we would expect to see little Faraday rotation and depolarization there. The density limits for these more realistic field configurations would be a few times larger than those given by equations (4) and (5) for cases (i) and (ii), respectively. The number of reversals, N , in the fully disordered case could be very large.

Even in the case of a fully ordered field, these limits are fully consistent with the densities inferred from our conservation-law analysis on the assumption that the thermal electrons originate entirely from entrained plasma with

normal cosmic abundances: $n \approx 0.7 \text{ m}^{-3}$, also at a projected distance of 28 arcsec from the nucleus (Laing & Bridle 2002b).

3 OVERVIEW OF THE ANALYSIS

3.1 Description

We seek to interpret the depolarization and Faraday rotation results in terms of the magnetic field structure in the Faraday-rotating medium, first by deriving the two-dimensional statistics of the magnetic-field fluctuations that produce the observed Faraday rotation (Section 4) and then by constructing models of three-dimensional distributions of gas and magnetic field which are consistent with these statistics (Section 5).

Our analysis proceeds in three stages:

(i) The two-dimensional fluctuations of Faraday rotation measure on scales larger than the observing beamwidth can be quantified in several ways. We will justify use of the RM structure function (Section 4.2) as the principal statistic. This restricts us to regions small enough that lateral variations of the foreground density and rms field strength can be neglected. Our approach is to guess a form for the magnetic power spectrum, derive the corresponding RM structure function (modified by the observing beam) and compare it with the data, estimating errors for the poorly-sampled large separations by making a set of artificial RM images with the theoretical power spectrum sampled on the same grid as our data.

(ii) Residual depolarization can be used to estimate the variations of Faraday rotation across the beam (Burn 1966; Tribble 1991a), thus extending the range of spatial scales we can study. We evaluate the depolarization expected from different power spectra numerically, by making finely-sampled realisations of RM images, which we then use to generate artificial polarization maps at the observing resolution.

(iii) For a large-scale foreground medium, the variations of RM fluctuation amplitude and depolarization with position depend on the orientation of the source (Garrington & Conway 1991; Tribble 1992). Knowing the density distribution from the X-ray observations and the geometry, the strength of the magnetic field can be estimated by fitting to the observed distributions using analytical single-scale models (e.g. Felten 1996), appropriately weighted estimates of the autocorrelation function or power spectrum (Enßlin & Vogt 2003; Vogt & Enßlin 2005) or three-dimensional simulations (Murgia et al. 2004; Govoni et al. 2006; Guidetti et al. 2008). We use simulations, incorporating constraints on the magnetic-field power spectrum from (i) and (ii). Unique features of our analysis are that the orientation of 3C 31 (at least close to the nucleus) is well determined and we have enough data to test whether the Faraday-rotating medium is spherically symmetric with a radial profile related to the density of the surrounding hot plasma.

The advantage of the approach using two-dimensional RM and depolarization analyses [steps (i) and (ii)] is that when making artificial RM images, we can use large computational grids to sample a full range of spatial scales accurately and

efficiently, reserving three-dimensional simulations for studies which include global variations of density and magnetic-field strength. We can also use the Hankel transform relation (Section 4.2.1) to predict the structure function expected for a given power spectrum, allowing explicitly for the effects of the observing beam.

3.2 Simplifying assumptions

We make a number of simplifying assumptions, as follows.

(i) Faraday rotation is produced entirely by a foreground screen. We have argued in Section 2.3 that this is a very good approximation for 3C 31.

(ii) The magnetic field is a Gaussian random variable, and its spatial distribution can therefore be described by the power spectrum or its Fourier transform, the autocorrelation function. This may well be incorrect if the field is intermittent, e.g. in the form of flux tubes or filaments (Eilek & Owen 2002, and references therein), but our data are too sparse to allow us to determine higher-order correlations.

(iii) The field is isotropic, in the sense that it has no preferred direction when averaged over a sufficiently large volume. Our data show no evidence for a preferred direction in the RM distribution on scales $\lesssim 100$ arcsec, but we note that this may not always be the case: for example the RM distributions in M 84 (Laing & Bridle 1987) and 3C 465 (Eilek & Owen 2002) appear to have banded structures. We do see RM gradients on very large scales in 3C 31, but these are consistent with sampling of an isotropic magnetic power spectrum with significant amplitude on these scales together with spatial variations in density.

(iv) The amplitude of the magnetic-field power spectrum varies with the thermal gas density in the foreground screen, which is in turn a smooth function of position. The form of the power spectrum, in contrast, is independent of position. We test this assumption by evaluating the spatial statistics in different regions of the source.

The importance of these assumptions is that the power spectra of the magnetic field and RM are then proportional (Enßlin & Vogt 2003). We work in terms of spatial frequency $\mathbf{f} = (f_x, f_y, f_z)$ with $\mathbf{f}_\perp = (f_x, f_y)$ in the plane of the sky. In the isotropic case, we can define the three-dimensional magnetic power spectrum $\hat{w}(f)$ such that $\hat{w}(f)df_xdf_ydf_z$ is the power in a volume $df_xdf_ydf_z$ of frequency space.²

Similarly, the two-dimensional RM power spectrum $\hat{C}(f_\perp)$ is defined such that $\hat{C}(f_\perp)df_xdf_y$ is the RM power for an element df_xdf_y . For a foreground screen of uniform depth and constant electron density, $\hat{w}(f)$ and $\hat{C}(f_\perp)$ are simply related [equation (A6)]. If the electron density and the normalization of $\hat{w}(f)$ vary significantly along the line of sight but not perpendicular to it, the functional forms of $\hat{w}(f)$ and $\hat{C}(f_\perp)$ are still identical (Enßlin & Vogt 2003). Thus we may use the RM structure function evaluated over limited areas to determine the *form* of $\hat{w}(f)$, but estimating

² Note that some authors use the one-dimensional form $4\pi f^2 \hat{w}(f)$. For the three-dimensional form, as used in this paper, a Kolmogorov power spectrum is $\hat{w}(f) \propto f^{-11/3}$ whereas the one-dimensional form is $4\pi f^2 \hat{w}(f) \propto f^{-5/3}$.

its *normalization* as a function of position requires a three-dimensional analysis.

4 TWO-DIMENSIONAL ANALYSIS

4.1 Choice of analysis technique

Our goal is to characterise the RM over areas of the radio source where the parameters which define its spatial statistics do not vary significantly. Descriptions in terms of spatial or frequency variables are equivalent and several different techniques have been used in the literature. One approach is to work directly in frequency space (Enßlin & Vogt 2003; Vogt & Enßlin 2003) to determine the power spectrum. Real-space alternatives are:

- (i) the *autocorrelation function*

$$C(r_{\perp}) = \langle \text{RM}(\mathbf{r}_{\perp} + \mathbf{r}'_{\perp}) \text{RM}(\mathbf{r}'_{\perp}) \rangle$$

(Enßlin & Vogt 2003; Vogt & Enßlin 2003) and

- (ii) the related *structure function* defined by:

$$S(r_{\perp}) = \langle [\text{RM}(\mathbf{r}_{\perp} + \mathbf{r}'_{\perp}) - \text{RM}(\mathbf{r}'_{\perp})]^2 \rangle$$

(e.g. Simonetti, Cordes & Spangler 1984; Leahy 1987; Minter & Spangler 1996).

Here, the vectors \mathbf{r}_{\perp} and \mathbf{r}'_{\perp} are again in the plane of the sky and $\langle \rangle$ denotes an average over \mathbf{r}'_{\perp} , defined by the area of the radio source. For a stationary random process, the structure and autocorrelation functions are related by $S(r_{\perp}) = 2[C(0) - C(r_{\perp})]$, although in practice, this relation will be approached only if the largest scale of fluctuations is significantly smaller than the size of the measurement area.

We work in real space and use the structure function rather than the autocorrelation function for the following reasons:

(i) Most of the useful properties of the autocorrelation function only appear when $C(r_{\perp})$ drops to 0 at some outer scale small compared with the sampled area. If this is not the case (as in 3C 31), the form of the function can vary wildly, typically oscillating with large amplitude at large separations.

(ii) A related point is that sensible use of the autocorrelation function requires an accurate knowledge of the zero level. This is uncertain for 3C 31: we have argued that the mean RM in the North tail is primarily Galactic, but there could still be significant contributions from local material. The zero-level for a particular region cannot be determined merely by averaging in the presence of large-scale fluctuations.

(iii) This problem is made worse by the irregular shapes of the sampling regions in 3C 31. This leads to particular problems with the frequency-space approach, as the corresponding window functions (Enßlin & Vogt 2003) are very complicated.

(iv) By comparison, the structure function $S(r_{\perp})$ is independent of the mean level and (to first order) of structure on scales larger than the measurement area.

$S(r_{\perp})$ is therefore relatively robust and can use all of the available evidence without giving systematic biases at the largest separations.

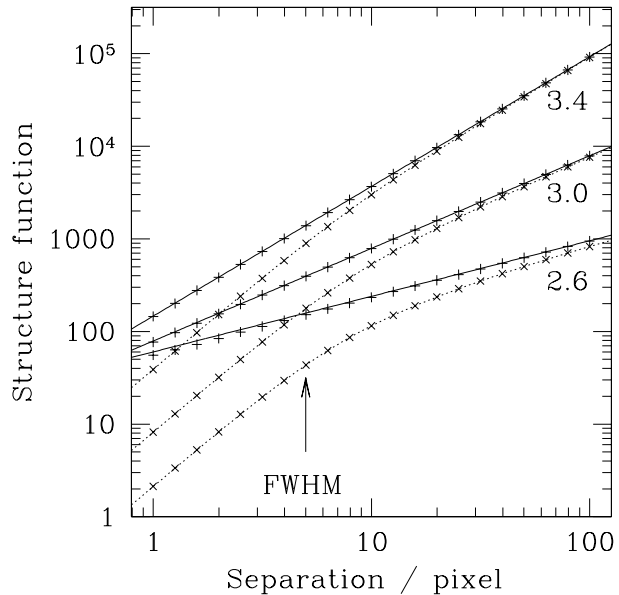


Figure 10. Full lines: plots of the structure functions corresponding to power spectra $\hat{C}(f_{\perp}) \propto f_{\perp}^{-q}$ (for $p = 2.6, 3.0$ and 3.4) over an infinite frequency range, from equation (B1). Dotted: structure functions for the same power spectra, but for images convolved with a Gaussian of FWHM 5 pixels [equation (B2)]. The crosses are the results of numerical integration. The agreement between analytical and numerical results is very good except for the case of a flat power spectrum without convolution, where there are small but significant errors at small separations (this case is not relevant to the observations, however).

4.2 Theoretical structure functions

4.2.1 Hankel transform relations

For isotropic fluctuations, the RM power spectrum $\hat{C}(f_{\perp})$ is the Hankel transform of $C(r_{\perp})$. Using the Fourier transform convention of Bracewell (2000),

$$C(r_{\perp}) = 2\pi \int_0^{\infty} \hat{C}(f_{\perp}) f_{\perp} J_0(2\pi f_{\perp} r_{\perp}) df_{\perp} \quad (6)$$

where $\hat{C}(f_{\perp})$ depends only on the scalar spatial frequency f_{\perp} .³ In the short-wavelength limit for a beam of FWHM = $2\sigma(\ln 2/\pi)^{1/2}$, the relation becomes

$$C(r_{\perp}) = 2\pi \int_0^{\infty} \hat{C}(f_{\perp}) f_{\perp} J_0(2\pi f_{\perp} r_{\perp}) \times \exp(-2\pi\sigma^2 f_{\perp}^2) df_{\perp} \quad (7)$$

4.2.2 Power-law power spectra and the effects of the observing beam

In what follows, we use finite frequency intervals and therefore need to evaluate the Hankel transform integrals [equations (6) and (7)] numerically. As a test of our procedure, Fig. 10 shows a comparison of analytical and numerical estimates for structure functions corresponding to power-law $\hat{C}(f_\perp)$ for an infinite frequency range, both before and after Gaussian convolution of the image. The analytical expressions are given in equations (B1) and (B2).

The effects of convolution on the observed structure function are very noticeable, especially for flat power spectra. For example, the structure function for $q = 2.6$ deviates significantly from its asymptotic form even for separations $r_\perp \approx 5 \times \text{FWHM}$ (Fig. 10). After convolution, the structure function approaches $S(r_\perp) \propto r_\perp^2$ for small r_\perp (Section B2).

4.3 Realisations of the RM distribution

4.3.1 Method

Errors for the structure function of poorly sampled data are impossible to evaluate analytically: they are correlated between adjacent position bins and depend on the details of the window function, particularly for large separations. For these reasons, we choose to generate multiple realisations of Gaussian random RM fields with given power spectra on the observed grids. The dispersion in the structure functions calculated for these realisations gives an estimate of the errors and allows us to determine the range of scales over which the observed structure functions are reliable. Our method for generating a realisation of a Gaussian random variable with a particular power spectrum is as follows.

(i) Make an array in the frequency plane whose elements are complex numbers whose real and imaginary parts are random numbers selected from a Gaussian distribution with zero mean and unit variance.

(ii) Multiply the elements of this array by the square root of the power spectrum, $[\hat{C}(f_\perp)]^{1/2}$.

(iii) Optionally, multiply by the Fourier transform of the convolving beam.

(iv) Perform a two-dimensional inverse Fourier transform to the image plane.

(v) Evaluate the structure function.

This was implemented using a FFT routine on a grid of size $n = 2^m$, setting implicit limits $1/n \leq f_\perp \leq 1/2$ to the maximum and minimum frequencies which can be sampled in either dimension (the upper limit is the Nyquist frequency). In practice, we used $n = 8192$ to ensure that the difference between the structure functions for minimum frequencies of 0 and $1/n$ is negligible over the range of spatial separations sampled by our data.

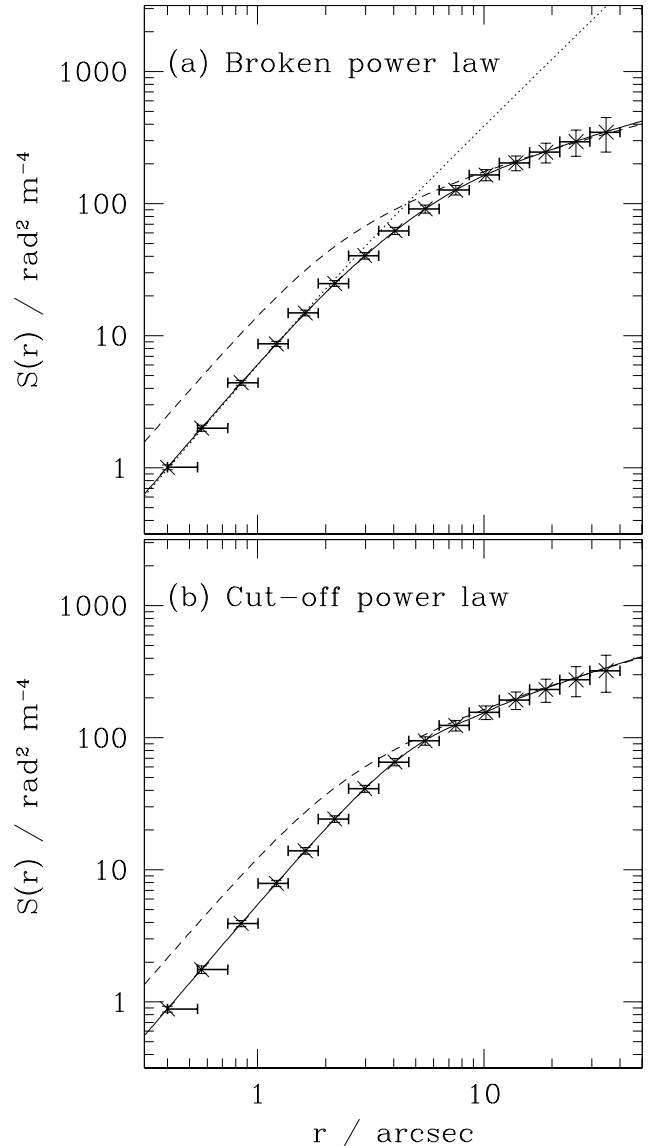


Figure 11. Comparison of structure functions derived by simulation and Hankel transform for an observing beam of 1.5 arcsec FWHM. (a) Broken power-law with indices $q_{\text{high}} = 11/3$, $q_{\text{low}} = 2.32$ and a break frequency $f_b = 0.062 \text{ arcsec}^{-1}$ [equation (8)]. (b) Power law with index $q = 2.39$ and a high-frequency cut-off at $f_{\text{max}} = 0.144 \text{ arcsec}^{-1}$ [equation (9)]. The full lines are the Hankel transform relations [equation (7)], assuming no low-frequency cut-off in the power spectrum. The points and error bars are derived from 100 realisations of the power spectrum on a 8192^2 grid with the sampling appropriate for region NP1. The horizontal bars represent the bin widths and the crosses the mean separation for data included in each of the bins. The error bars represent the rms variations for the model structure functions. The dashed curves are the structure functions for pure power-law power spectra with the appropriate low-frequency indices [$q = 2.39$ and 2.32 respectively for panels (a) and (b)]. In panel (a), we also show the structure function for a power-law power spectrum with $q = 11/3$ (dotted line).

4.3.2 Modified power-law $\hat{C}(f_{\perp})$

In order to fit the observed structure functions, we require power spectra of the cut-off and broken power-law forms given in equations (8) and (9), below. For both cases, we have verified that the mean of the structure functions from realisations of the power spectrum converges to the Hankel transform result and that the finite size of the grid for the realisations has a negligible effect on the structure functions for the separations we sample. Example calculations for both types of structure function are shown in Fig. 11.

4.4 Observed structure function

The areas of 3C 31 where we have enough contiguous data points to evaluate the RM structure function are disconnected from each other and have very different variances. We have therefore analysed the areas NP1, SP1 and SP2 (Fig. 3c) separately at 1.5-arcsec resolution. Use of the 5-frequency, 5.5-arcsec RM image (Fig. 2c) allows us to examine the larger areas NP2 and SP3, but adds little extra information for NP1 and SP1, where essentially all of the emission is detected at the higher resolution (SP2 and SP3 overlap). Systematic errors are likely to be important for SP2: the signal-to-noise ratio is relatively low and independent RM fitting algorithms give significantly different structure functions. We plot the data for this region, but do not use them in our determination of the form of the structure function.

In the presence of noise, the structure function has a positive bias, and for uncorrelated random noise with rms σ_{fit} , its expectation value is $2\sigma_{\text{fit}}^2$. We have made a first-order correction for this bias by evaluating $S(r_{\perp}) = S_{\text{raw}}(r_{\perp}) - 2\sigma_{\text{fit}}^2$, where $S_{\text{raw}}(r_{\perp})$ is the structure function determined directly from the images and σ_{fit} is set to be the rms error in the RM for the area in question. In practice, σ_{fit} lies between 1.6 and 3 rad m^{-2} so the correction is small in the North and insignificant in the South. The noise is essentially uncorrelated on scales larger than the beam. The measured structure functions for the 5 regions are shown in Fig. 12(a) – (e); in Fig. 12(f), we show a superposition of the structure functions for all three southern regions.

We have investigated the hypothesis that the power spectrum (and hence the structure function) has the same form for all of the regions, but with varying normalization. It is clear from Fig. 12 and from Figs 9(a) and (b) that there is significant power on a range of spatial scales and that a Gaussian power spectrum, (for which we expect a flat structure function on large scales) is inadequate. Motivated by the approximately power-law form for the structure function and equation (B1), we initially tried an RM power spectrum of the form $\hat{C}(f_{\perp}) \propto f_{\perp}^{-q}$ over an infinite frequency range. Even after including the effects of the beam [equation (B2), Fig. 10], the model structure functions showed insufficient curvature to fit our 1.5-arcsec resolution data: all three regions imaged at 1.5-arcsec resolution require a change in

structure-function slope at $r_{\perp} \approx 10$ arcsec; this is also apparent from the superposition of data for the South of the source in Fig. 12(f). Two functional forms for $\hat{C}(f_{\perp})$ which have been discussed in the literature and which fit the data reasonably well are a *broken power law* (hereafter BPL)

$$\begin{aligned} \hat{C}(f_{\perp}) &= D_0 f_b^{-11/3} (f_{\perp}/f_b)^{-q_{\text{low}}} & f_{\perp} \leq f_b \\ &= D_0 f_{\perp}^{-11/3} & f_{\perp} > f_b \end{aligned} \quad (8)$$

and a *cut-off power law* (hereafter CPL)

$$\begin{aligned} \hat{C}(f_{\perp}) &= C_0 f_{\perp}^{-q} & f_{\perp} \leq f_{\text{max}} \\ &= 0 & f_{\perp} > f_{\text{max}} \end{aligned} \quad (9)$$

The former is motivated by the expectation that the power spectrum will have a Kolmogorov form on small scales. Fig. 11 compares the structure functions expected for the high- and low-frequency asymptotic forms of these power spectra with those corresponding to equations (8) and (9), emphasising that there must be a change in slope over the observable frequency range.

For each region, we optimised the normalization over a grid of models specified by q_{low} and f_b for BPL and q and f_{max} for CPL. In order to estimate the errors from undersampling, we made multiple realisations of convolved RM images corresponding to the BPL model power spectrum on the observed grid and evaluated the rms deviations of their structure functions. These represent the errors expected purely from statistical fluctuations in the absence of noise or systematic errors if the model power spectrum is valid everywhere. They are much larger than the errors expected from the RM fits, and we therefore used them to evaluate chi-squared, which we then summed over all bins with separation $> \text{FWHM}$ as a measure of the goodness of fit. Note, however, that the errors for adjacent bins are not independent.

In Table 1, we quote the optimised parameters for NP2, NP1, SP1 and SP3 separately. Uncertainties are approximate 1σ (68% confidence) limits for two interesting parameters. Acceptable fits have tightly correlated values of q_{low} and f_b (or q and f_{max}), so we quote pairs of values defining the extrema of contours of constant chi-squared.

We then determined a best overall fit by minimising chi-squared summed over all four regions, giving equal weight to each and allowing the normalizations to vary independently. We find best-fitting parameters of $q_{\text{low}} = 2.32$ and $f_b = 0.062 \text{ arcsec}^{-1}$ for the BPL model and $q = 2.39$ and $f_{\text{max}} = 0.144 \text{ arcsec}^{-1}$ for the CPL model. The corresponding structure functions, including the effects of the convolving beam, are plotted in Fig. 12, where the amplitudes have been scaled as in Table 2 to fit the observations (we also include the fit for SP2). The rms deviations from multiple realisations are plotted as error bars attached to the observed points.

Fig. 12 shows that the observed structure functions for NP2, NP1, SP1 and SP3 are in very good agreement with the models. Together with the absence of any compelling evidence for non-Gaussianity, anisotropy or correlation with the small-scale structure of the source (confirmed by visual comparison between example realisations, such as those in Fig. 13, and the data), this indicates that our model power

³ Note that Enßlin & Vogt (2003) use wavenumber rather than spatial frequency and a different Fourier transform convention, but their power spectra are the same as ours with the substitution $f_{\perp} = k_{\perp}/2\pi$.

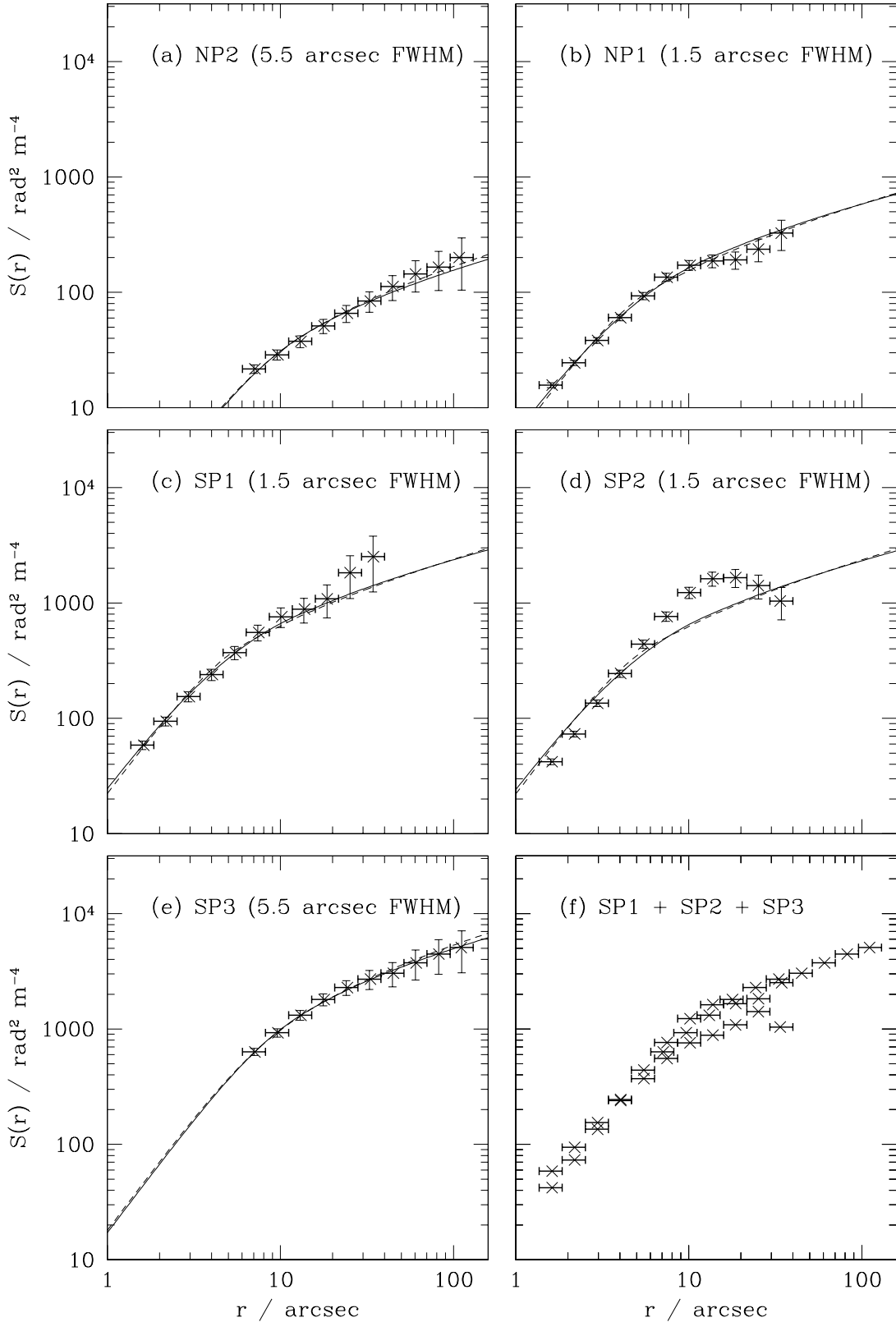


Figure 12. (a) – (e): plots of the RM structure function for the regions indicated in Figs 2 and 3. The horizontal bars represent the bin widths and the crosses the mean separation for data included in the bins. The curves are the predictions for the model power spectra described in the text, including the effects of the convolving beam. The full and dashed curves denote the broken and cut-off power-law models, respectively. The error bars represent the rms variations for structure functions derived using the broken power law power spectrum on the observed grid of points for each region. Panel (f) shows the superposition of structure functions for all three regions in the South of the source.

Table 1. Structure function parameters for individual regions and for a combined fit to all four regions. The last line of the table refers to the combined fit in which the values of q_{low} and f_{b} (or q and f_{max}) are the same for all regions, but the individual normalizations are varied to minimise the overall chi-squared (these normalizations are listed in Table 2).

Region	FWHM arcsec	BPL						CPL					
		Best fit		Min slope		Max slope		Best fit		Min slope		Max slope	
		q_{low}	f_{b}	q_{low}	f_{b}	q_{low}	f_{b}	q	f_{max}	q	f_{max}	q	f_{max}
NP2	5.5	2.35	0.178	2.14	0.062	2.54	∞	2.34	0.231	2.10	0.086	2.55	∞
NP1	1.5	1.84	0.051	-0.2	0.034	2.45	0.076	2.35	0.148	2.00	0.122	2.62	0.190
SP1	1.5	2.76	0.073	0.50	0.024	3.10	0.155	2.89	0.210	2.46	0.126	3.12	∞
SP3	5.5	2.27	0.049	1.70	0.026	2.51	∞	2.32	0.083	2.03	0.058	2.63	∞
Comb		2.32	0.062	2.15	0.053	2.47	0.072	2.39	0.144	2.28	0.134	2.49	0.156

spectra are acceptable representations of the observed RM fluctuations. The hypothesis that only the amplitude of the power spectrum varies with position is therefore consistent with our results, especially given that the approximation of constant path length through a region inevitably introduces some inaccuracies (these are corrected in the 3-d simulations of Section 5). A more rigorous error analysis (best done using a Bayesian maximum likelihood technique, e.g. Vogt & Enßlin 2005) is outside the scope of this paper.

The BPL model fits the combined observations very slightly better, and we adopt it as our standard, but we cannot differentiate between the two functional forms (or similar ones) using our RM data alone. The two model power spectra have almost the same form at low spatial frequencies. The CPL form predicts $S(r_{\perp}) \propto r^2$ at small separations (Section B2), quite close to the asymptotic $r^{5/3}$ expected for the Kolmogorov spectrum [equation (B1)], which is itself steepened by the effects of convolution. In Fig. 14, we show the two power spectra and their associated structure functions. The latter are almost identical, particularly after convolution (Figs 14d and f), explaining our inability to distinguish between them. The power in fluctuations on scales $\lesssim 5$ arcsec differs significantly for the two models, however (Fig. 14b) so in Section 4.5 we attempt to use the measured depolarizations at 1.5-arcsec resolution to select between them.

4.5 Constraints from observed depolarization and the validity of the short-wavelength approximation

Measurement of residual depolarization constrains the amplitude of RM fluctuations on scales smaller than the beam. In order to test consistency with our adopted model for the power spectrum and to check whether the fitted RM is close to the convolution of the true RM distribution with the beam [the short-wavelength approximation of equation (1)], we proceed as follows.

- (i) We make realisations of the RM distributions for our adopted power-spectrum parameters on a fine grid (0.05 arcsec pixels) and scale the amplitude as appropriate.
- (ii) We then calculate Q and U at each of our observing frequencies for a uniformly polarized source.
- (iii) We convolve the resulting images to the observing

Table 2. Normalizations D_0 and C_0 for the combined fit parameters from Table 1. Observed and calculated depolarization are also given for regions NP2, NP1, SP1 and SP3. 1: region name. 2: normalization constant D_0 for the model power spectrum of equation (8). 3: normalization constant C_0 for the model power spectrum of equation (9). 4: Observed Burn law $\langle k \rangle$, with errors. Only data with $p > 4\sigma_p$ are included, and for NP1 and SP1 we only include points within 60 arcsec of the nucleus. 5: $\langle k \rangle$ predicted for the BPL power spectrum. 6: As 5, but for the CPL power spectrum. Rms sampling errors for the models are also given in columns 5 and 6.

Region	D_0	C_0	$\langle k \rangle / \text{rad}^2 \text{m}^{-4}$		
			Observed	BPL	CPL
NP2	0.019	0.61	46 ± 8	21.8 ± 0.7	23.2 ± 0.8
NP1	0.064	1.9	3 ± 7	14.7 ± 0.1	9.7 ± 0.3
SP1	0.26	7.8	55 ± 13	59.7 ± 0.9	40.0 ± 1.1
SP2	0.25	7.7			
SP3	0.61	19	372 ± 18	569 ± 13	542 ± 7

resolution and derive the polarized power $P = (Q^2 + U^2)^{1/2}$ and \mathbf{E} -vector position angle, χ .

(iv) We then fit χ against λ^2 and $\ln p$ against λ^4 to make images of RM and k as for the observations.

(v) We average over the images to derive the mean values of the Burn parameter $\langle k \rangle$ and the degree of polarization $\langle p(\lambda) \rangle$ at each of our observing wavelengths.

(vi) Finally, we compare the derived RM image with the convolution of the full-resolution version with the observing beam.

We have verified that the short-wavelength approximation holds to high accuracy for the model power spectra in regions NP1, NP2, SP1 and SP2 by taking the differences between simulated RM images and convolutions of the true RM distributions with the appropriate observing beams. The rms difference is $< 0.1 \text{ rad m}^{-2}$ (negligible compared with the noise) and the means differ by $< 0.01 \text{ rad m}^{-2}$ in all four regions. Even in SP3, where the short-wavelength approximation breaks down, the mean structure function for a large number of simulated RM images is in precise agreement with that derived from the Hankel transform relation. The reason is that areas of high depolarization and deviation

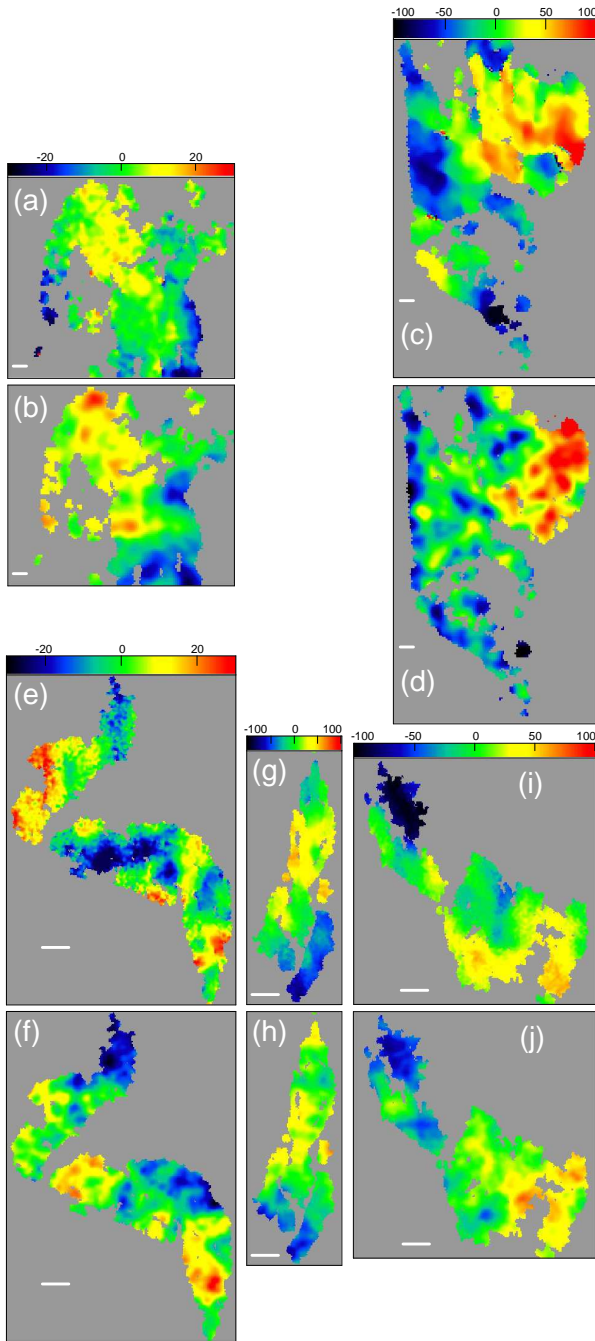


Figure 13. A comparison between the RM data in the regions used for structure-function analysis and example realisations generated using the BPL power spectrum described in the text. The mean values for each panel were subtracted before plotting to facilitate comparison of smaller-scale structure. The normalizations are given in Table 2. (a) and (b): data and model for region NP2. (c) and (d): SP3; (e) and (f): NP1; (g) and (h): SP1; (i) and (j): SP2. Note that noise in the RM fits is generally uncorrelated on small scales, and the observed RM images therefore appear to have slightly more small-scale structure than the models. This is more obvious in panels (a), (b), (e) and (f), where the amplitude of the noise relative to the plotting range is larger. The colour scales ($\pm 30 \text{ rad m}^{-2}$ for panels a, b, e and f); $\pm 100 \text{ rad m}^{-2}$ for the remaining plots) are shown by labelled wedges. The horizontal lines give a scale of 10 arcsec.

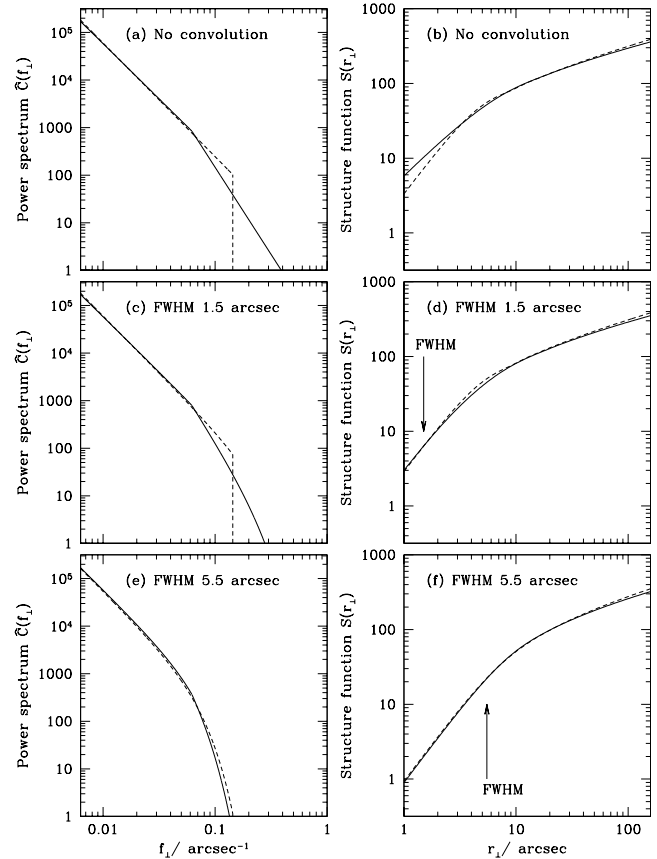


Figure 14. (a), (c), (e): the two model RM power spectra discussed in the text. Solid line, BPL with indices $q_{\text{high}} = 11/3$, $q_{\text{low}} = 2.32$ and a break frequency of $0.062 \text{ arcsec}^{-1}$ [equation (8)]. Dashed line: CPL with $q = 2.39$ and a high-frequency cut-off at $f_{\text{max}} = 0.144 \text{ arcsec}^{-1}$ [equation (9)]. (b), (d), (f): structure functions computed for the power spectra in panels (a), (c) and (d), with the same line codes. (a) and (b) no convolution; (c) and (d) 1.5 arcsec FWHM convolving beam; (e) and (f) 5.5 arcsec FWHM convolving beam.

from λ^2 rotation occupy a small fraction of the RM image and therefore have very little effect on the spatial statistics (see Appendix C for a more detailed analysis of these effects).

The mean values $\langle k \rangle$ predicted for regions NP1 and SP1 by the BPL [equation (8)] and CPL [equation (9)] models for $\hat{C}(f_{\perp})$ are given in Table 2. Both models predict values consistent with the observations, so we cannot use the measured depolarization to discriminate between them. In Figs 15(a) and (b), we compare the observed mean degrees of polarization at our six observing wavelengths with the predictions of the BPL model derived directly from multiple realisations and find very good agreement (the CPL model again gives very similar results).

In regions NP2 and SP3, where we have only low-resolution data, the predicted variations of $\langle p \rangle$ with λ are not in such good agreement with the observations (Table 2). For NP2, we predict slightly too much depolarization [Fig. 15(c)]. The observed degree of polarization does not fall monotonically with increasing wavelength, however, indicating either that the approximation of constant intrinsic polarization is invalid or that we have underestimated the sys-

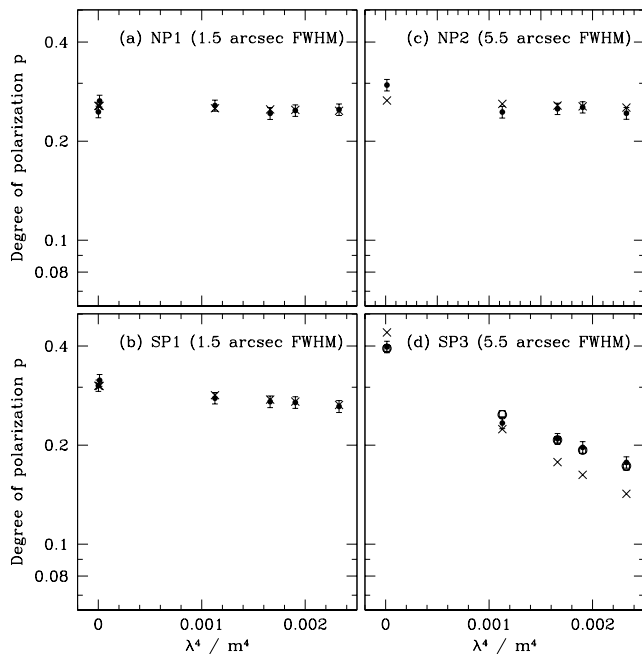


Figure 15. Plots of the degree of polarization (on a log scale) against λ^4 for the regions: (a) NP1, (b) SP1, (c) NP2 and (d) SP3. The filled circles with error bars represent the observed mean degrees of polarization. The crosses show the predicted variations of polarization with wavelength for the BPL model with the amplitudes from Table 2. Panel (d) also shows predicted values for the BPL models with $D_0 = 0.38$ and $f_b = 0.062 \text{ arcsec}^{-1}$ (open squares) and $D_0 = 0.61$ and $f_b = 0.037 \text{ arcsec}^{-1}$ (open circles). The predicted values for these two cases are almost identical, so the symbols appear superposed. In all cases, the intrinsic degree of polarization, $p(0)$, has been set to give the best agreement (minimum chi-squared) between predicted and observed values.

tematic errors. In contrast, we predict significantly more depolarization in SP3 than is observed [Fig. 15(d)]⁴. We show in that figure that we can reproduce the run of polarization with wavelength by simple modifications to the parameters of the BPL power spectrum, for example, by reducing the amplitude to $D_0 = 0.38$ but keeping the break frequency and low-frequency slope at the values in Table 1 or by maintaining the amplitude and slope at low spatial frequencies but decreasing the break frequency to $f_b = 0.037 \text{ arcsec}^{-1}$. These discrepancies suggest that the form as well as the amplitude of the RM power spectrum may vary slightly across the source, but we cannot quantify the variation further without higher-resolution observations of the RM fluctuations in the low-surface-brightness regions NP2 and SP3.

4.6 The outer scale and autocorrelation lengths

We have so far implicitly assumed that the outer scale of the magnetic-field and RM fluctuations is large compared with the size of the regions over which we evaluate the structure function. This is justified by the fact that the structure functions continue to rise with increasing separation

Table 3. Magnetic autocorrelation lengths for the broken and cut-off power-law models [equations (8) and (9), respectively]. The model used for three-dimensional simulations is the broken power law (BPL) with $f_{\min} = 0.00075 \text{ arcsec}^{-1}$.

f_{\min} arcsec^{-1}	λ_B / kpc	
	BPL	CPL
0.005	4.9	2.8
0.001	9.0	5.7
0.00075	10.0	6.5

up to $r_{\perp} \approx 100 \text{ arcsec}$. The outer scale cannot be arbitrarily large, however, and its value has important implications for the estimation of magnetic-field strength and autocorrelation length.

Our constraints on the outer scale of the magnetic-field fluctuations from the structure-function analysis are weak, because of the poor sampling of large separations. For both the broken and cut-off power law models, we infer $f_{\min} \lesssim 0.005 \text{ arcsec}^{-1}$ in regions NP2 and SP3. If the apparent RM gradient over $\sim 800 \text{ arcsec}$ (Fig. 9a) is due to large-scale structure in the local field (rather than a gradient in Galactic RM) then $f_{\min} \lesssim 0.001 \text{ arcsec}^{-1}$. The autocorrelation lengths for the magnetic field [λ_B ; equation (A4)] and RM [λ_{RM} ; equation (A5)] depend on the outer scale. Equations (A7) and (A8) allow us to determine the autocorrelation lengths for both model power spectra analytically; values of λ_B for three representative minimum frequencies are given in Table 3.

4.7 Origins of the power spectrum

There is no generally accepted theory of magnetic-field fluctuations in intra-cluster plasma, although a turbulent cascade from large to small scales is expected. Dissipation of turbulence is predicted to occur on the resistive scale, which is far below our resolution limit (e.g. Schekochihin & Cowley 2006). Energy input might come from sub-cluster mergers or galaxy motions within the group and from interactions between the radio source and the surrounding plasma. Possible input scales L range from $L \approx 25 \text{ kpc}$ (the projected separation between NGC 383 and its nearest neighbour and the bending radius of the inner jets) to $L \approx 500 \text{ kpc}$ (the total size of the radio source). The magnetic power spectrum is expected to have a power-law form with slope $q = 11/3$ over some inertial range if the turbulence is primarily hydrodynamic (Kolmogorov 1941) or for the type of MHD cascade analysed by Goldreich & Sridhar (1997). Our results show that the power spectrum could have this form on scales $\lesssim 5 \text{ kpc}$, but must flatten on larger scales. Such a break in slope might occur at a characteristic field reversal scale $l_{\perp} \sim 0.01 - 0.1L$ if the field is generated by some form of fluctuation dynamo (Schekochihin & Cowley 2006; Enßlin & Vogt 2006).

⁴ The observed and predicted depolarizations at longer wavelengths in SP3 are less pronounced than predicted by the Burn law, as first pointed out by Tribble (1991a).

5 THREE-DIMENSIONAL MODELS

5.1 General considerations

We have established that essentially all of the Faraday rotation associated with 3C 31 is due to foreground material (Section 2.3). The only known ionized gas component with the requisite scale size is the hot plasma associated with the surrounding group of galaxies, which is centred close to 3C 31 (Komossa & Böhringer 1999). Although a component of Faraday rotation associated with a thin shell of material around the lobes of extragalactic radio sources has been postulated by Bicknell, Cameron & Gingold (1990, see also Rudnick & Blundell 2003), this component cannot dominate, as there would then be no reason for the path lengths to differ between the approaching and receding lobes. There would then be no explanation for the systematic asymmetry in RM variance and/or depolarization with jet prominence seen in 3C 31 and many other FRI sources (Morganti et al. 1997). Cooler ($\sim 10^4$ K) ionized gas has been detected only in the inner few arcsec of 3C 31 (Owen, O’Dea & Keel 1990; Noel-Storr et al. 2003) and may be expected to clump on scales much smaller than those of the observed large-scale RM gradients. We therefore model the Faraday rotation as an effect of magnetic field distributed throughout the group gas.

5.2 Simulations with a realistic power spectrum

Realistic predictions of the RM distribution can be made using Monte Carlo simulations. Our method is essentially that of Murgia et al. (2004): as in our two-dimensional analysis, we assume that the magnetic field is an isotropic, Gaussian random variable. To construct a numerical realisation of such a magnetic field in a cubical box, we start from a magnetic vector potential $\mathbf{A}(\mathbf{r})$ with a given power spectrum (Tribble 1991b).

(i) At each point of a $2^m \times 2^m \times 2^m$ grid in frequency space, we select the real and imaginary parts of the vector components of the Fourier transform of the vector potential $\hat{\mathbf{A}}(\mathbf{f})$ from a Gaussian random distribution with unit variance.

(ii) We then multiply by the square root of the power spectrum of the vector potential. For a magnetic-field power spectrum $\hat{w}(f) \propto f^{-q}$, this is $\propto f^{-q/2}$.

(iii) Our 2-d analysis was consistent with a magnetic power spectrum which has the same form everywhere, but varying normalization, so all of the 3-d simulations assume the BPL power spectrum of equation (8) with $q_{\text{low}} = 2.32$ and $f_b = 0.062 \text{ arcsec}^{-1}$. The minimum frequency is set to $f_{\text{min}} = 0.00075 \text{ arcsec}^{-1}$, matching the size of the sampling grids. The magnetic autocorrelation length is $\lambda_B = 29.6 \text{ arcsec}$ (10.0 kpc).

(iv) The corresponding magnetic field in Fourier space, $\hat{\mathbf{B}}(\mathbf{f}) = 2\pi i \mathbf{f} \times \hat{\mathbf{A}}(\mathbf{f})$, is then divergence-free.

(v) We transform the line-of-sight field component B_z to real space and multiply it by the assumed density function $n(\mathbf{r})$ to generate a Faraday depth model.⁵

(vi) nB_z can then be integrated along the line of sight

from the emitting surface to the front surface of the cube to generate a simulated RM image.

(vii) Finally, we convolve the RM image with the observing beam, assuming that the short-wavelength approximation holds, and sample it as for the observations.

In practice, we used 512^3 and 1024^3 grids for the low- and high-resolution images, respectively, with cell sizes in real space set to 2.6 and 1.3 arcsec. For each of the models described below, we made 25 realisations at low resolution, allowing us to explore the variation in predicted profiles, together with one realisation at high resolution. We have verified that we recover the input power spectrum from two-dimensional structure-function analyses for regions over which the fluctuation amplitudes are reasonably uniform.

5.3 Comparison between predicted and observed RM distributions

Our criterion for an acceptable 3-d model is that it fits both the form and the amplitude of the RM structure function to within errors set by a combination of sampling variance and noise in the observations. In order to assess the goodness of fit, we need to average over areas which are small enough to resolve spatial variations but large enough to give robust estimates of the RM fluctuation amplitude. Our approach is to make binned profiles of σ_{RM} at 5.5 arcsec resolution from the multiple realisations (sampled in the same way as the observations) and then to optimise the overall normalization. Our measure of goodness of fit is chi-squared, summed over all bins with a significant number of points. As errors, we use the rms of the fitting error for the observations (from the least-squares analysis of Section 2.3) and the sampling error for the simulations (from the multiple realisations), combined in quadrature. We have fit both the 4 and 5-frequency RM profiles. The simulations are more tightly constrained by the latter, whose fitting errors are significantly smaller.

Our assumptions are as follows:

- (i) The two sides of the source are intrinsically identical.
- (ii) The emitting and Faraday-rotating media are axisymmetric with an axis orientated at 52.4° to the line of sight, as in the model of Laing & Bridle (2002a) for the inner jets.
- (iii) The surrounding gas density distribution has a radial density profile as characterised by Komossa & Böhringer (1999), with a central density of 1900 m^{-3} , a core radius of $r_c = 52 \text{ kpc}$ and a form factor $\beta_{\text{atm}} = 0.38$. We ignore the effects of the gas component associated with the galaxy (Hardcastle et al. 2002, see below). We distinguish two types of model:

Spherically symmetric The source can be represented as a plane containing the inner jet axis, i.e. it has negligible extent along the line of sight. This is physically unrealistic, as we expect thermal matter to be excluded from the volume occupied by the relativistic plasma, but should be a good approximation where the source is narrow, and is a useful comparison with earlier work (Garrington & Conway 1991; Tribble 1992).

⁵ As noted by Murgia et al. (2004), this does not precisely pre-

Cavity Thermal plasma is excluded from the volume occupied by relativistic plasma, as expected from theoretical models (e.g. Scheuer 1974). Cavities apparently devoid of X-ray emitting material are indeed observed around some *FRI* sources (e.g. McNamara & Nulsen 2007, and references therein) We have experimented with various geometries, and show the results for ellipsoidal cavities.

(iv) The normalization of the RM power spectrum then depends only on the density $n(r)$ and the rms field $B(r)$. We assume that the magnetic field is given by $B \propto n^\mu$. We consider a range from $\mu = 0.1 - \mu = 1.5$. $\mu = 0.5$ corresponds to equipartition of magnetic and thermal energy and was assumed by Garrington & Conway (1991); $\mu = 2/3$ is expected for flux-freezing and $\mu \approx 1$ is consistent with the correlation of X-ray surface brightness and RM variance for clusters of galaxies (Dolag et al. 2001; Dolag 2006). The best-fitting values of B_0 and μ are correlated for any model, since a higher value of μ gives a relatively lower Faraday rotation at large distances from the nucleus, requiring an increase in central field strength.

We show the results for the spherically-symmetric and cavity models in Sections 5.4 and 5.5, respectively.

5.4 Spherically-symmetric distributions of density and field

Figs 16(a) and (b) show the comparison between the observed profiles of σ_{RM} and those for the spherically-symmetric model. The best fit has a central rms magnetic-field strength, $B_0 = 0.28$ nT ($2.8 \mu\text{G}$) and $\mu \approx 0.5$. The fit is poor: chi-squared for the 5-frequency profile is 35.7 with 6 degrees of freedom. Fits of similar quality are obtained for any μ in the range $0.1 \lesssim \mu \lesssim 0.8$.

The model profiles show an asymmetry in RM fluctuation amplitude, but the variation (which occurs on a scale $\sim r_c$) is much slower than observed. The predicted RM fluctuation amplitude is systematically too high (by a factor of two) in the North. It also falls rapidly in the South lobe at distances $\gtrsim r_c \approx 150$ arcsec (following the density profile), and therefore fails to match the observed value at ≈ 300 arcsec from the nucleus.

The failure of this model to fit the remarkably low RM fluctuation amplitude in the North of 3C 31 is graphically illustrated by a comparison between example realisations and the observations [Figs 17(a) – (d)]. Corresponding profiles of mean RM at two resolutions and rms RM at 1.5 arcsec resolution only are shown in Figs 18(a) – (f).

5.5 Cavities

We have estimated the effect of cavities on the RM variation assuming that they are evacuated volumes that do not perturb the surrounding gas or field. We first examined the effect of “minimal” cavities that match the inner jets as modelled by Laing & Bridle (2002a), continued outwards. These are cones with half-opening angle 13.2° centred on and extending to a distance of 50 arcsec from the nucleus, after which they become cylindrical. The effect of these “minimal” cavities on the RM distribution in a spherically symmetric model was too small to be detectable. In

order for a cavity model to generate the observed rapid RM gradient across the nucleus, we found that: (a) the initial half-opening angle of the cavities must exceed that of the inner radio jet, and (b) the cavities must enclose a volume somewhat larger than that of the high-brightness structure from which our RM images are derived.

A simple model which significantly improves the fit has ellipsoidal cavities as sketched in Fig. 19. These have semi-major and semi-minor axes of 252 arcsec (85 kpc) and 200 arcsec (68 kpc), respectively. The semi-major axis projects to 200 arcsec on the plane of the sky. The best fit is for $\mu \approx 1.0$ [Figs 16(c) and (d)]. Example realisations and profiles are shown in Figs 17(e) and (f) and Figs 18(g) – (i), respectively. The low level of RM fluctuations in the North is reproduced quite well, but there is still a significant difference between the observed 5-frequency and simulated profiles (chi-squared = 18.6 with 6 degrees of freedom). This is due mostly to one bin, at 300 arcsec from the nucleus in the South and coincident with the most negative RM values in the source [Figs 2(b) and (c)]. The central bins give relatively small contributions to the total chi-squared, despite the large differences between observed and predicted values, because the sampling errors are large where the source is narrow. The 4-frequency profiles of σ_{RM} are formally consistent with the cavity model for any μ in the range $0.1 \lesssim \mu \lesssim 1.2$ and the chi-squared for $\mu = 1.0$ is 7.0 with 8 degrees of freedom.

For this model, the rms central magnetic-field strength is $B_0 = 0.74$ nT ($7.4 \mu\text{G}$). This is larger than for the spherically-symmetric model because there is a lower Faraday depth at large radii for given B_0 , partly as a consequence of the steeper radial field dependence ($\mu = 1.0$), but mainly because there is less gas along the line of sight. Both effects require an increase in normalization to match the observed Faraday rotation in the South at large radii. The X-ray gas parameters were determined by fitting to azimuthally averaged profiles, however (Komossa & Böhringer 1999). In the presence of a cavity with the shape we assume, the central density would be underestimated by a factor ≈ 1.5 and the inferred field strength would be overestimated by the same factor.

The predicted σ_{RM} profiles are generally insensitive to the precise shape of the cavity provided that it extends to the full extent of the sampled region and has a half-opening angle comparable with the angle to the line of sight, $\theta \approx 52^\circ$; for example we have generated similar fits for a cavity which initially expands in a cone, becoming cylindrical far from the nucleus. The best-fitting value of μ depends on the precise shape of the cavity, since both affect the Faraday depth at large radii.

Although our simple axisymmetric cavity model gives a reasonable fit to the observed RM distribution, reality is likely to be much more complicated:

(i) The cavity required to fit the RM data appears much larger than the observed extent of the brightest synchrotron emission at 1.4 GHz near the nucleus. We note, however, that there is low-brightness emission from the North and South spurs close to the nucleus and within the projected envelope of the cavity. This is visible within 200 arcsec of the nucleus on the East side of both jets (Figs 1 and 19).

(ii) It is also possible that earlier epochs of source activity

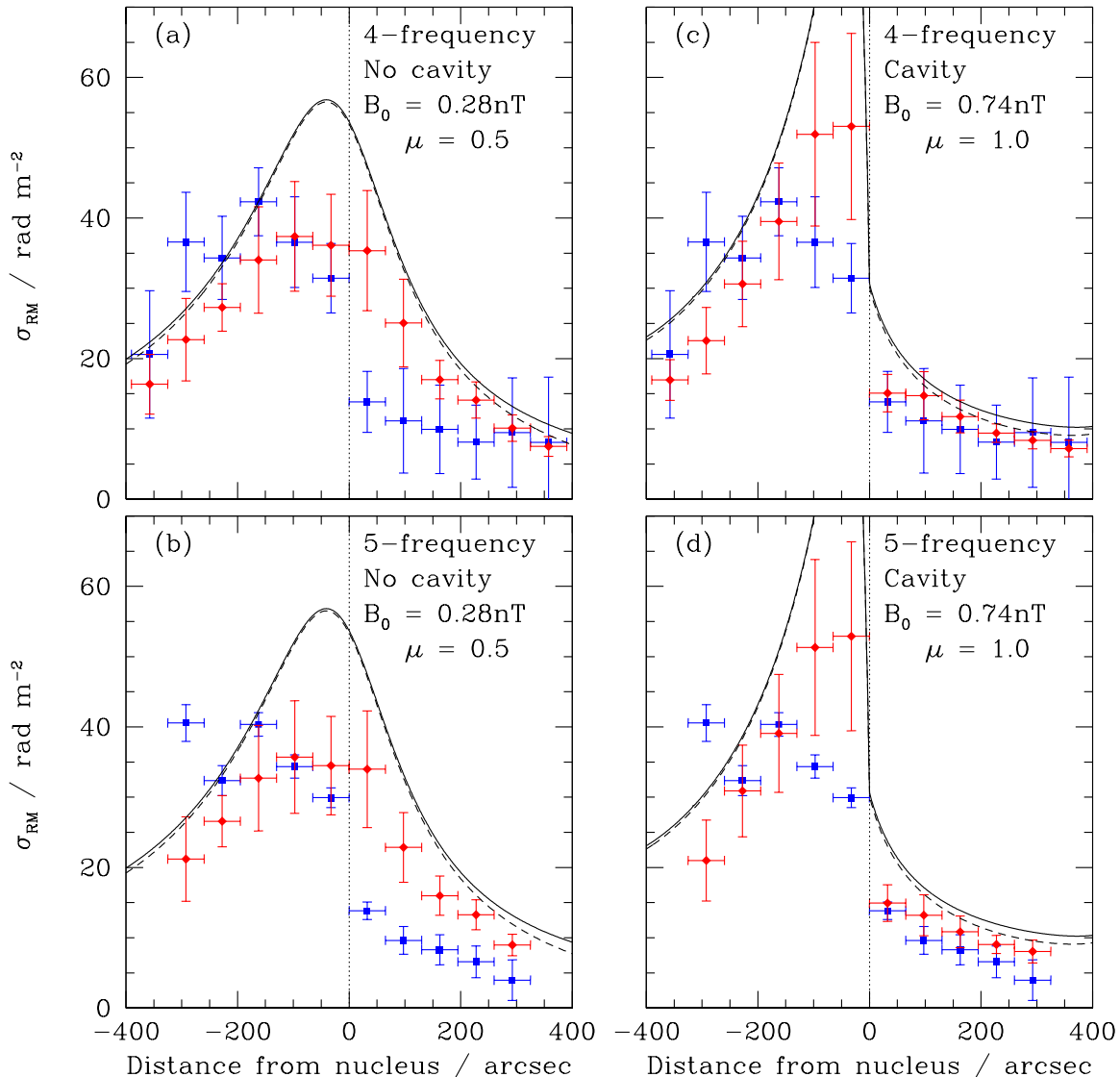


Figure 16. Comparison of observed and simulated profiles of rms Faraday rotation measure σ_{RM} at 5.5 arcsec resolution. The blue squares represent observed values, with vertical bars corresponding to the rms errors on the RM fit. The red diamonds show the mean values from 25 simulated profiles and the vertical bars represent the rms scatter in these profiles. The normalizations of the model profiles have been determined by chi-squared minimisation. The curves are the predictions of a single-scale model with $D = \lambda_B$, as described in Section 5.7. The full curve is for an infinite upper integration limit and the dashed line corresponds to truncation of the integral at the near surface of the simulation volume. (a) and (b): 3-d model with spherical symmetry (Sec. 5.4). The central rms field strength is $B_0 = 0.28$ nT and $\mu = 0.5$. (c) and (d): 3-d model with cavity geometry (Sec. 5.5), $B_0 = 0.74$ nT and $\mu = 1.0$.

could have cleared a bigger volume of thermal matter. Such a cavity would not have been detected in existing *Chandra*, *ROSAT* or *XMM-Newton* X-ray images (Hardcastle et al. 2002; Komossa & Böhringer 1999; Croston et al. 2008), but should be clearly visible in a longer *XMM-Newton* integration or, in the radio, at lower observing frequencies (cf. Birzan et al. 2008).

(iii) Alternatively, the surprisingly large size required for the cavities may just be an artefact of the simplicity of our model. Clearly, we cannot constrain the shape of the cavities along lines of sight where there is no polarized emission. Our inference of a large transverse size for the cavities projected on the plane of the sky is purely a consequence of the shape of the σ_{RM} profile in those areas we can sample and

the assumptions of axisymmetry and identical cavities. It is possible that the cavities are significantly larger along the line of sight than transverse to it or that they differ radially from each other in shape. In particular, the structure of 3C 31 as projected on the plane of the sky is not straight, so it is likely that bends also occur in the plane defined by the source axis and our line of sight. Such bending might well modify the Faraday depth distribution on large scales.

(iv) If significant magnetoionic material is associated with other galaxies in the NGC 383 group located in front of the radio emission from 3C 31, we might expect to see additional, localized, Faraday rotation. An additional contribution to the rms RM at a distance of ≈ 300 arcsec from the nucleus in the South would greatly improve the σ_{RM} fit, so

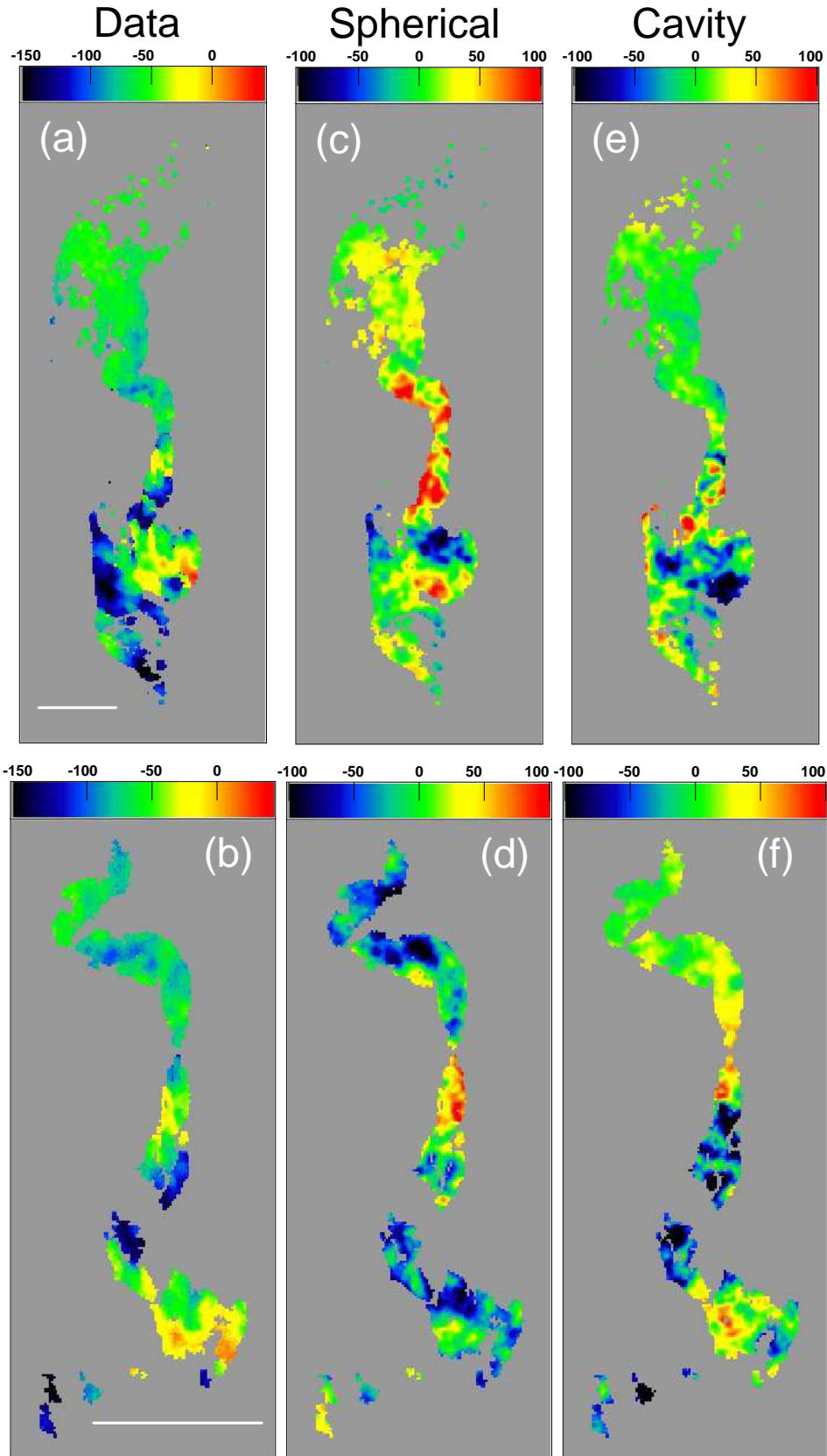


Figure 17. Comparison of observed and simulated distributions of Faraday rotation measure RM at 5.5 and 1.5 arcsec resolutions. (a) and (b): observed. (c) and (d): 3-d model with spherical symmetry (Sec. 5.4). (e) and (f): 3-d model with cavity geometry (Sec. 5.5). The colour scale is the same for all displays but the RM scales for the data are offset by the Galactic RM contribution (Section 2.4). The bar at the base of panels (a) and (b) shows a 100 arcsec scale.

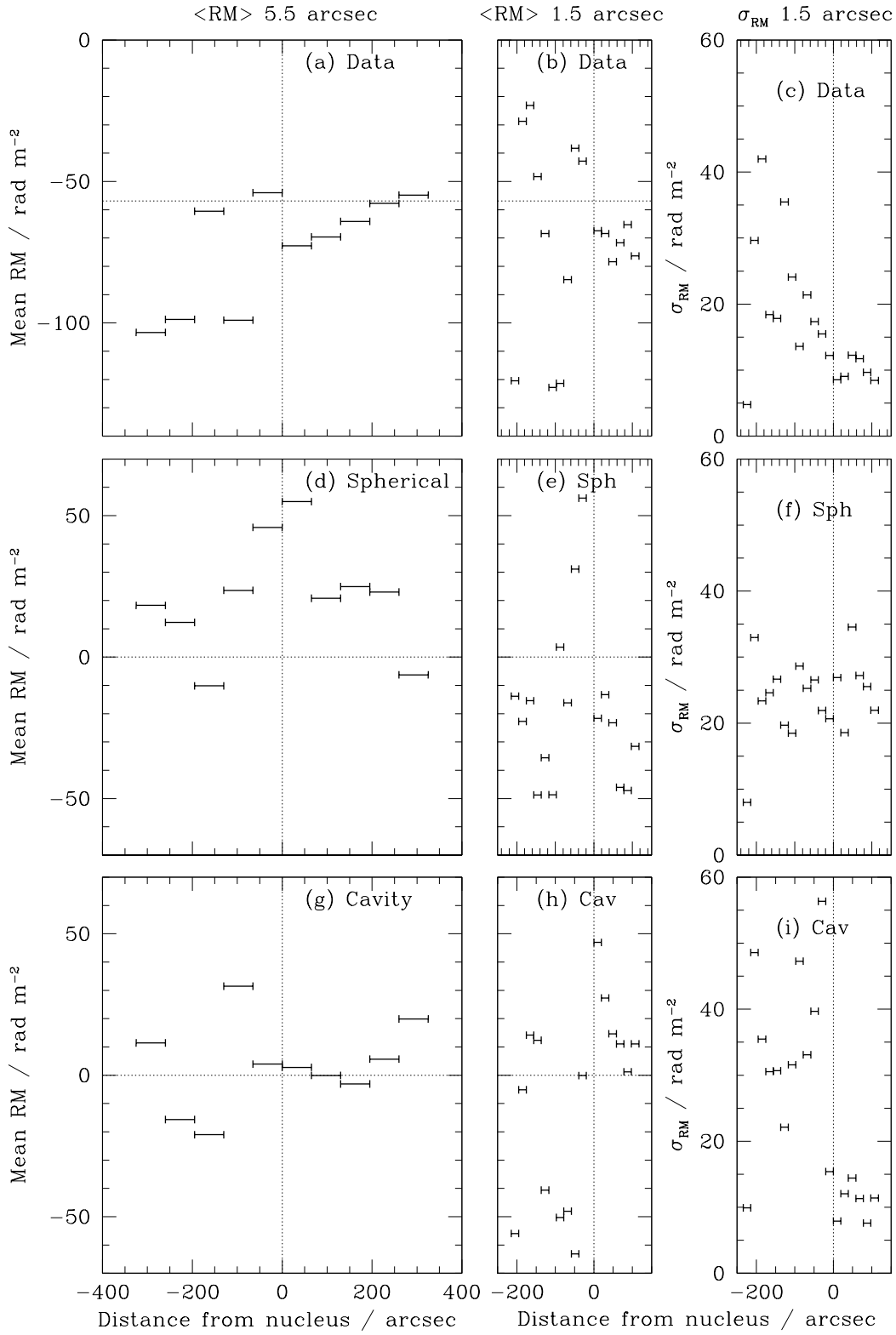


Figure 18. Observed and simulated profiles of $\langle \text{RM} \rangle$ and σ_{RM} , with the same binning as in Fig. 9. The observed data at 5.5 arcsec resolution are from the 5-frequency fits [Fig. 2(c)] and the simulated profiles correspond to the example realisations shown in Fig. 17. (a) – (c): observed; (d) – (f): 3-d model with spherical symmetry (Sec. 5.4); (g) – (i): 3-d model with cavity geometry (Sec. 5.5). Panels (a), (d) and (g) show the mean RM values at 5.5 arcsec resolution; (b), (e) and (h) show mean values at 1.5-arcsec resolution and (c), (f) and (i) give the rms RM at the higher resolution.

we searched for foreground galaxies close to the RM anomaly in the South on the Digital Sky Survey. No candidate objects are found within ≈ 2 arcmin, however.

(v) There could be an entirely “accidental” large-scale intrinsic asymmetry in the foreground Faraday screen that produces an excess RM over the outer South jet and tail, coincidentally reinforcing the RM asymmetry for the inner regions. Some intrinsic asymmetries must be present in the gas distribution to provide the observed bending of the radio structure, the different shapes of the radio spurs and tails in the North and South, and the flat edge of the East side of the South spur (Laing et al. 2008, and this paper, Fig.1). A large-scale asymmetry is also evident in the *ROSAT* image, in which the nucleus of 3C 31 is displaced by ≈ 1 arcmin to the North-East of the centre of the group gas distribution (Komossa & Böhringer 1999).

(vi) Finally, our interpretation of the RM profiles close to the nucleus might be complicated by Faraday rotation associated with the galaxy-scale hot gas component imaged by Hardcastle et al. (2002), which has a core radius of only 3.6 arcsec. If this had the same field strength and power spectrum as we assume for the group gas, then there would be a large excess RM close to the nucleus. We have estimated the resulting σ_{RM} profile and find that there would be a detectable excess between -20 and $+15$ arcsec, a factor of two increase between -12 and $+10$ arcsec and a peak of $\sigma_{\text{RM}} \approx 400 \text{ rad m}^{-2}$ within ≈ 1 arcsec of the nucleus (positive and negative distances refer to the main (North) and counter (South) jets, respectively). We have no information about lines of sight within a beamwidth of the nucleus, which is unpolarized for our observing frequencies and resolutions (perhaps because of such large Faraday rotation gradients on small scales). We see no evidence of anomalously high RM’s close to it, however. In any case, we have no reason to suppose that the field strength and power spectrum we have adopted are appropriate for the galaxy-scale component, which is smaller than the magnetic autocorrelation length we derive for the group gas. We can therefore justify our neglect of the galaxy-scale component, noting that it may affect the innermost bins of Fig. 18.

These considerations suggest that it may not be possible – or necessary – to explain every feature of the large-scale Faraday RM distribution over 3C 31 with a symmetric model of the magnetoionic medium. Nevertheless, we have demonstrated that such a model can provide an approximate fit to our RM observations and we certainly cannot ascribe the entire asymmetry to “accidental” effects and still preserve its correlation with jet sidedness in the FR I population as a whole.

5.6 Alternative explanations for the RM asymmetry

Our inference of large cavities surrounding the radio structure is testable by deeper radio and X-ray observations. If these cavities are not detected, alternative ways to produce a Faraday depth distribution consistent with our data must be considered.

One possibility is that the magnetic field is anisotropic. A locally two-dimensional structure is expected either if the field is “draped” over the surface of a subsonically-expanding

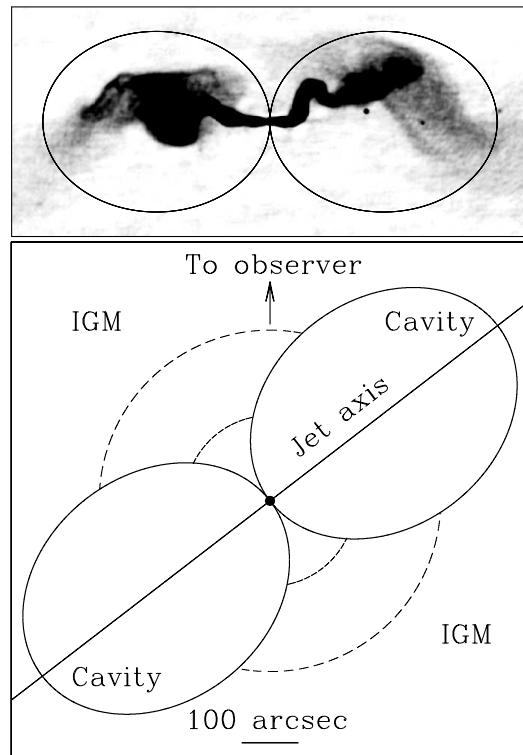


Figure 19. The assumed cavity geometry for 3C 31. Top: the cavity shape that produced the best fit to the RM data projected on a total-intensity image and rotated so the inner jet axis is horizontal. Bottom: a cross-section through the cavity in the plane defined by the jet axis and the line of sight. The dashed arcs of circles represent isodensity contours in the IGM.

lobe (Dursi & Pfrommer 2008) or if it is compressed by a bow-shock surrounding the source. This could introduce a systematic change in B_z/B with position and hence a gradient of RM fluctuation amplitude. For this mechanism to produce a gradient in the observed sense, a special geometry is needed: the two-dimensional field sheets in front of the approaching lobe must be preferentially orthogonal to the line of sight while those in front of the receding lobe are aligned with it. This might occur if the field is enhanced along surfaces that are oblique to the radio jet axis, as in a bow shock – such a structure might be imposed at some distance from the source by sound/shock waves created by earlier outbursts from the AGN (as seen in the Perseus cluster by Fabian et al. 2006, for example).

Alternatively, the Faraday-rotating material might be in a disk whose radius (after projection) is similar to, or larger than, the sampled area of the tail. A thin disk with a fairly uniform distribution of Faraday depth would naturally produce a steep gradient of RM fluctuation amplitude across the nucleus, coupled with the lack of variation across the outer South tail. One possibility is that the gas distribution itself is highly flattened. As an example, we have simulated an oblate beta-model gas disk with a large core radius containing a magnetic field and orientated roughly perpendicular to the radio axis. Such a disk could produce the flat profile of σ_{RM} in the South, but would also generate higher RM than observed in the inner North jet unless it is extremely thin. Flattened X-ray emitting gas distributions have occasionally

been observed around radio galaxies (e.g. Kraft et al. 2005), but the group X-ray source surrounding 3C 31 is quite round (Komossa & Böhringer 1999; Croston et al. 2008), inconsistent with the appearance of a highly inclined, thin disk. If the hot gas is responsible for the Faraday rotation but has a spherical distribution, then the only remaining possibility is that the magnetic field has a disk-like configuration, a supposition that seems entirely ad hoc.

Finally, the Faraday rotation might come from a different phase of the ionized IGM than that visualised by the X-ray data. Dusty ‘superdisks’ with diameters $\gtrsim 75$ kpc and thicknesses ≈ 25 kpc have previously been postulated to explain depolarization asymmetry and other properties of powerful radio galaxies (Gopal-Krishna & Nath 1997; Gopal-Krishna & Wiita 2000). Such a disk in 3C 31 would be too thick to show the rapid change in RM fluctuation amplitude across the nucleus that we observe and in any case the observed disk of molecular and ionized gas and dust is tiny by comparison with the scale of the observed Faraday rotation – ≈ 2 kpc in diameter (Martel et al. 1999; Okuda et al. 2005; Noel-Storr et al. 2003). This explanation for the Faraday-rotation asymmetry also seems extremely unlikely.

5.7 A note on single-scale models

A rough, but rapidly calculable, approximation to the profile of rms RM along the source axis can be derived from a single-scale model of the magnetic-field structure (Burn 1966; Felten 1996). The basic assumption is that the magnetic field is orientated randomly within cells of uniform size D and both the strength of the field and the thermal electron density are smooth functions of position. The rms foreground Faraday rotation σ_{RM} , can then be calculated by integrating the expression:

$$\sigma_{\text{RM}}^2 = \frac{K^2 D}{3} \int_{z_{\text{em}}}^{z_{\text{obs}}} B^2(z) n^2(z) dz \quad (10)$$

(Felten 1996) where z_{em} is the position of the front surface of the emitting material along the line of sight z and z_{obs} is the position of the observer (usually $z_{\text{obs}} \rightarrow \infty$). The integral does not generally have a solution in closed form, but we have verified that our numerical algorithm reproduces the analytical results derived by Felten (1996) in special cases. This method allows rapid computation of σ_{RM} profiles and we have used it extensively to explore different field and density combinations.

For quantitative modelling, the single-scale model has serious disadvantages, however. Although it can be used to derive a rough value of the field strength, the appropriate cell size D to use for a realistic power spectrum is not obvious. The apparent RM fluctuation scale, or more precisely the RM autocorrelation length λ_{RM} [equations (A5) and (A8)], is not the correct value. Murgia et al. (2004) showed that the approximation $D \approx \lambda_B$, where λ_B is the magnetic autocorrelation length [equations (A4) and (A7)] holds for power-law magnetic power spectra provided that σ_{RM} is measured over a sufficiently large area – a restriction which is not satisfied in our analysis of σ_{RM} profiles at 5.5 arcsec resolution close to the centre of the source. We have to limit the size of our averaging bins along the jets in order to resolve the

global variations of path length and RM. Close to the nucleus, the source structure is dominated by narrow jets, so there are only a few autocorrelation areas per bin (Table 3) and the single-scale model systematically overestimates the rms given by a full 3-d simulation (Fig. 16). At distances $\gtrsim 100$ arcsec, where the source broadens, the single-scale approximation with $D = \lambda_B$ gives a much better representation of the simulated profiles. Finally, we note that a full simulation is required in order to estimate errors for a realistic power spectrum and the sampling grid defined by the observations.

The single-scale approximation does, however, allow us to estimate the effects of the finite depth of the simulation volume on the simulated σ_{RM} profile by comparing the predictions of equation (10) with z_{obs} set to the half-width of the simulation box and $z_{\text{obs}} = \infty$. For the cases we have modelled in detail, the two profiles are very similar (Fig. 16), so almost all of the RM fluctuations will be accounted for by the 3-d simulation.

6 HYDRA A

Aside from 3C 31, Hydra A is the only FRI radio galaxy with a well-imaged RM distribution in which there is a pronounced asymmetry across the nucleus (Taylor & Perley 1993). In 3C 31, the orientation is well determined (at least near the nucleus) and the group gas is well characterised by X-ray observations, but our preferred explanation for the observed global RM distribution – that the radio lobes have inflated cavities which are devoid of thermal plasma – has not yet been adequately tested using X-ray observations. For Hydra A, the radio source orientation is less well determined, but the cavities associated with the inner radio lobes have been directly imaged using *Chandra* (McNamara et al. 2000; Wise et al. 2007). It is therefore of interest to examine how well a cavity model can account for the global RM variations over this source. As for 3C 31, we start by deriving the RM structure function (Section 6.1) and use the results to simulate the RM variations (Section 6.2).

6.1 Structure function

In order to derive an RM power spectrum for our simulations and to compare our results with the Bayesian maximum-likelihood method of Vogt & Enßlin (2005), we measured the RM structure function as in Section 4. We used RM images made using the AIPS RM task (Taylor & Perley 1993) and the PACERMAN algorithm (Vogt, Dolag & Enßlin 2005), as in Section 2.4. We evaluated the structure function for the North lobe of Hydra A between 5 and 15 arcsec from the nucleus, where both algorithms are in good agreement.⁶ The results derived from the PACERMAN RM image are shown in Fig. 20. As noted by Vogt et al. (2005), there is significant uncorrelated noise in the RM image, and we have corrected the structure function for this using the noise estimates from that reference, as in Section 4.4.

⁶ In the South lobe, the RM’s are very large, there is significant depolarization and the RM distributions calculated using the two algorithms differ significantly. We have not, therefore, calculated the RM structure function in this part of Hydra A.

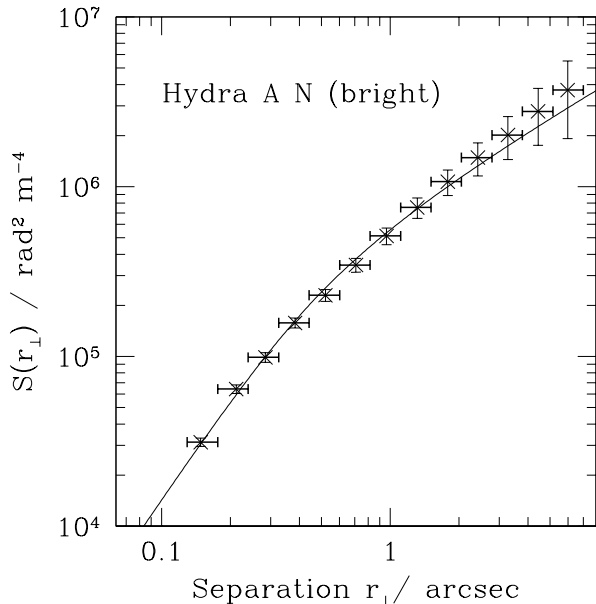


Figure 20. The RM structure function for the brightest region of the North lobe in Hydra A. The curve shows the predicted structure function, $S(r_{\perp})$, for a power-law RM power spectrum with slope $q = 2.77$ and a convolving beam of 0.3 arcsec FWHM. Error bars show the rms spread for multiple realisations of the model power spectrum.

We fit BPL and CPL models, again as in Section 4.4. Both fits gave the same solution: a pure power law with q_{low} (or q) = 2.77 ± 0.10 with no requirement for a break in slope or high-frequency cut-off within our (relatively limited) sampling range. The fitted structure function is shown in Fig. 20. BPL models with $f_b > 0.9 \text{ arcsec}^{-1}$ (0.8 kpc^{-1}) are allowed by the data for $q_{\text{low}} \approx 2.7$, however. In contrast, Vogt & Enßlin (2005) found a Kolmogorov spectrum for $f \gtrsim 0.32 \text{ kpc}^{-1}$, flattening at lower frequencies (but they did not include the effect of the convolving beam, FWHM = 0.32 kpc, in their analysis).

Thus we find that the index of the power spectrum for Hydra A ($q \approx 2.8$) is steeper than the low-frequency index for 3C 31 ($q_{\text{low}} \approx 2.3$). Assuming a BPL power spectrum, the break frequency is at $f_b \approx 0.2 \text{ kpc}^{-1}$ for 3C 31 compared with $f_b \gtrsim 0.8 \text{ kpc}^{-1}$ for Hydra A.

6.2 Distribution of magnetoionic material

We attempted to reproduce the large-scale variations over a composite RM image of Hydra A made using the PACERMAN algorithm for the North lobe, as in Section 6.1, and the AIPS RM task for the South lobe, where the PACERMAN solution is questionable (Vogt et al. 2005). There is substantial depolarization in the South, and the AIPS RM image also contains a number of artefacts such as large discontinuities on scales smaller than a beam. In order to reduce these problems, we blanked all points with RM outside the range -15000 to $+10000 \text{ rad m}^{-2}$ and those below a total-intensity threshold. The composite RM image is shown in Fig. 21(a).

We characterised the background density distribution using the double beta model of Wise et al. (2007), normal-

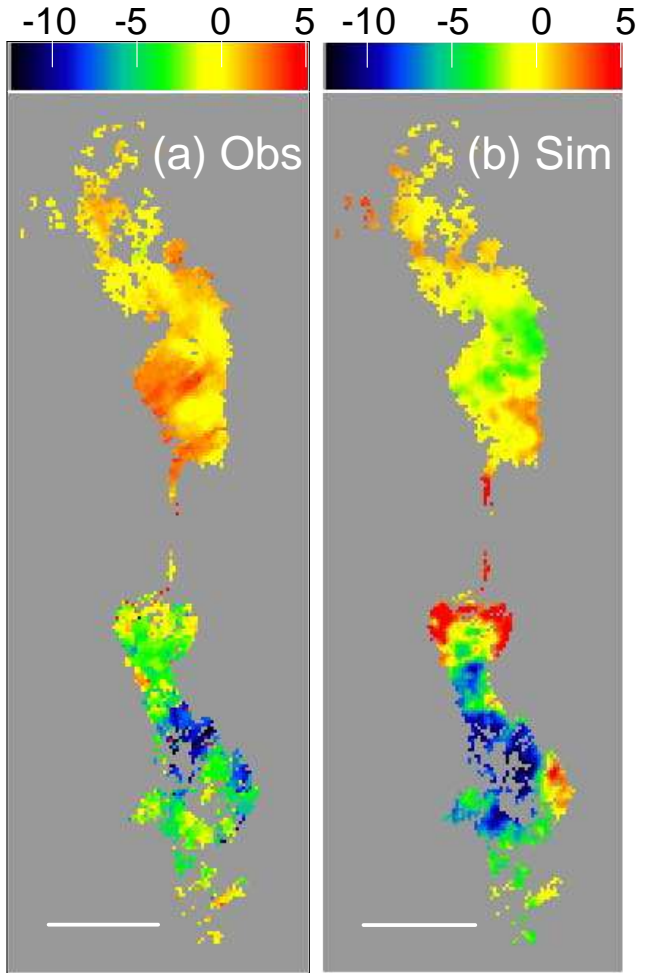


Figure 21. Observed and simulated RM images for Hydra A. (a) Observed RM, using data from Taylor & Perley (1993). The RM's for the North and South lobes are from Vogt et al. (2005) and Taylor & Perley (1993), respectively. (b) A simulation using a power-law RM power spectrum with index $q = 2.77$. The assumed angle to the line of sight is 45° , $B \propto n^{0.25}$ ($\mu = 0.25$) and the density model includes cavities A and B from Wise et al. (2007) as described in the text. The RM scale is from -12500 to 5000 krad m^{-2} . The images have been rotated clockwise by 26° compared with those in Taylor & Perley (1993) and Vogt et al. (2005) and the resolution is 0.3 arcsec FWHM. The horizontal bars indicate a scale of 20 kpc (18.7 arcsec).

ized to the deprojected profile of David et al. (2001). The parameters of the model are given in Table 4. We approximated the shapes of the inner two cavities A and B (Wise et al. 2007) as identical ellipsoids with projected semi-major axes of 19.8 arcsec exactly along the jet and semi-minor axes of 11.8 arcsec centred at projected distances of 24.1 arcsec on either side of the nucleus. These are the mean values for the two cavities given by Wise et al. (2007); A and B are on opposite sides of the nucleus, but otherwise very similar in geometry and location. Our simulations were as described for 3C 31 in Section 5.2, but taking a power-law magnetic power spectrum with $q = 2.77$, as derived in Section 6.1 and an upper frequency limit of $f_{\text{max}} = 1.67 \text{ arcsec}^{-1}$, set by the size of the simulation grid (512^3 with 0.3-arcsec pixels). We also fixed the lower frequency limit to be $f_{\text{min}} = 0.012 \text{ arcsec}^{-1}$.

f_{\min} is poorly constrained by our structure-function data, but the presence of large-scale RM variations across the 80-arcsec inner structure of Hydra A (Taylor & Perley 1993) requires the power spectrum to have significant amplitude at this frequency.

As the inclination of Hydra A is not well determined, we simulated angles to the line of sight in the range $37.5^\circ \leq \theta \leq 60^\circ$ – larger values failed to generate the observed RM asymmetry and smaller ones are improbable given the size of the source and its relatively low jet/counter-jet ratio (Taylor et al. 1990). We also varied the dependence of magnetic field strength on density, taking $B \propto n^\mu$ with $0.1 \leq \mu \leq 1.0$. For each pair of values θ, μ , we generated 25 realisations. We then compared the observed and simulated profiles of σ_{RM} , binning in boxes of length 4.2 arcsec along the jet axis (PA 26° on the sky) and extending to cover the entire width of the source. Finally, we adjusted the central rms field strength to optimise the agreement between observed and simulated profiles, using a combination of fitting and sampling errors to define chi-squared, just as for 3C 31.

There is a well-defined minimum in chi-squared, with best-fitting values of $\theta = 45^\circ$ and $\mu = 0.25$. The 68% confidence region is an ellipse in the θ, μ plane with semi-major axes $\sigma_\theta \approx 7^\circ$ and $\sigma_\mu \approx 0.2$. The agreement between observed and predicted profiles of σ_{RM} for the best fit is good [Fig. 22(a); chi-squared = 12.7 with 14 degrees of freedom]. In particular, the large difference between the fluctuation amplitudes in the two lobes is reproduced well, whereas a spherically-symmetric model without cavities gives an unacceptable fit for any inclination. As in 3C 31, the discrepancies close to the nucleus are not significant: errors on the predicted values are large because of poor sampling in the region of the narrow inner jets. We show an example realisation in Fig. 21(b). This has been chosen to illustrate that the change in sign of RM observed on large scales can be generated naturally by our assumed power spectrum without the need to postulate an additional ordered component of magnetic field (cf. Taylor & Perley 1993). Figs 22(b) and (c) show profiles of observed and predicted mean RM.

The changes in RM amplitude across Hydra A in this picture are due almost entirely to the inner beta model, whose core radius is 27.7 kpc (26.5 arcsec) and to the cavity structure. Any RM fluctuations due to the larger and more tenuous gas component would be essentially constant in amplitude across the central 80 arcsec region which we consider. The observed fall-off in RM at distances $\gtrsim 20$ arcsec in the South lobe is consistent with the drop in density, as predicted but not seen in the corresponding (South) lobe of 3C 31.

The central magnetic field strength required to match the RM fluctuation amplitude for the 45° simulation with cavities is 1.9 nT, significantly larger than the 0.7 nT deduced from modelling of the North lobe alone by Vogt & Enßlin (2005). We have used the single-scale approximation with scale-length λ_B to compare our predicted profiles of σ_{RM} with those of Vogt & Enßlin (2005) and find very good agreement for the North lobe. The discrepancy in field strength therefore results from differences in the field and density models, as follows:

(i) The spherically-symmetric model used by

Table 4. Two-component density model assumed for simulations of RM in Hydra A. n_0 is the central density of a component, r_c is its core radius and β_{atm} is the form factor. $n(r) = n_0(1 + r^2/r_c^2)^{-3\beta_{\text{atm}}/2}$.

n_0 / m^{-3}	r_c / kpc	β_{atm}
6.2×10^4	27.7	0.686
2.6×10^2	235.6	0.907

Vogt & Enßlin (2005) predicts a significantly higher density than that of Wise et al. (2007) over the range of radii responsible for the bulk of the Faraday rotation.

(ii) Our inclusion of cavities further reduces the amount of gas along the line of sight compared with the expectation from a spherically symmetric model.

(iii) We find that $\mu \approx 0.25$ gives a better fit to the RM fluctuation profile for a density model with cavities, whereas Vogt & Enßlin (2005) estimate $\mu = 0.5$ for a spherically symmetric model.

(iv) The power spectrum derived by Vogt & Enßlin (2005) is significantly different from ours. In order to estimate the effect on the derived central field strength, we can compare the magnetic autocorrelation lengths. Vogt & Enßlin (2005) derive $\lambda_B = 1.5$ kpc [dividing by 2 to match our definition from equation (A4)], compared with 3.1 kpc for our model power spectrum.

Our results for Hydra A provide quantitative support for our picture of magnetic field distributed through a spherical background gas distribution with embedded cavities. In this source (the only case where the gas density and cavity structure are both well determined), we can match the global variation of RM fluctuation amplitude for plausible angles to the line of sight.

7 SUMMARY AND FURTHER WORK

7.1 Summary

We have analysed images of linearly polarized emission in the FRI radio galaxy 3C 31 with resolutions of 5.5 and 1.5 arcsec FWHM at six frequencies between 1365 and 8440 MHz. Our use of all six frequencies in an analysis of the variation of the degree of polarization with wavelength has enabled us to measure very small depolarizations, which we characterize using the Burn law parameter k . At 1.5-arcsec resolution, we find $\langle k \rangle = 3 \text{ rad}^2 \text{ m}^{-4}$ ($\text{DP}_{6\text{cm}}^{22\text{cm}} = 0.99$) within 60 arcsec of the nucleus in the North jet and $\langle k \rangle = 55 \text{ rad}^2 \text{ m}^{-4}$ ($\text{DP}_{6\text{cm}}^{22\text{cm}} = 0.88$) in the South. The low depolarization and absence of deviation from λ^2 rotation confirm that almost all of the observed Faraday rotation is due to foreground material. The RM fluctuation amplitude is significantly larger in the South.

The amplitude and scale of the RM fluctuations in 3C 31 appear qualitatively similar to those derived for other well-observed FRI sources in comparable environments, e.g. NGC 6251 and 3C 449 (Perley, Bridle & Willis 1984;

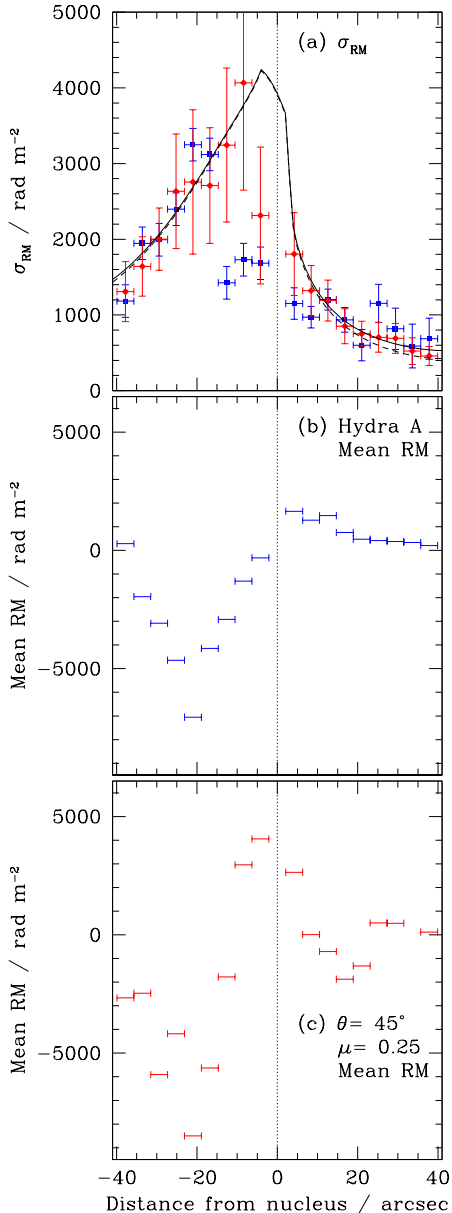


Figure 22. Profiles of RM along the inner jet axis for observed and simulated images of Hydra A (Fig. 21). The simulations assumed $\theta = 45^\circ$, $B_0 = 1.9$ nT and $\mu = 0.25$, with the geometry described in the text. Data have been averaged in boxes of length 4.2 arcsec along the jet axis, extending to cover the entire width of the source. The jet axis is taken to be vertical in Fig. 21 or PA 26° on the sky. Positive and negative distances refer to the North and South lobes, respectively (the former is approaching in the simulations). (a) rms RM. The observed values are indicated by the blue squares, with errors derived from the RM fits. The simulation results (red diamonds) represent the mean and rms scatter from 25 realisations. The curves show the predicted values of σ_{RM} for a single-scale model with $D = \lambda_B = 3.1$ kpc, as calculated for the model power spectrum. Full line: infinite integration range; dashed line: integration truncated at the near surface of the simulation box. (b) Observed mean RM. (c) Mean RM for the simulation shown in Fig. 21(b). This particular realisation (one out of 25) was chosen to illustrate that a large-scale change in sign of RM can be generated naturally by an isotropic magnetic field with the power spectrum we assume.

Feretti et al. 1999), but are much smaller in amplitude than those in FRI sources located in cD galaxies with cooling cores such as M 87 and Hydra A (Owen, Eilek & Keel 1990; Taylor & Perley 1993) and much larger than for NGC 315, which is in a sparse group (Laing et al. 2006a).

We have determined the RM structure function for five regions in 3C 31 over which the fluctuation amplitude is roughly constant. We model the fluctuations on the assumption that the magnetic field responsible for the foreground rotation is an isotropic Gaussian random variable (characterised entirely by its power spectrum). For the range of foreground Faraday rotation seen in 3C 31, the observed RM image is very close to the true image convolved with the observing beam. We have used this approximation to incorporate the effects of the beam in the calculation of theoretical structure functions for model power spectra by numerical integration of a Hankel transform relation. We evaluate errors due to imperfect sampling by making multiple realisations of the model power spectrum on the observed grid. For the four regions with the most reliable RM measurements, our data are consistent with an RM power spectrum which has the same form everywhere but whose amplitude varies with position. The power spectrum cannot be a single power law over the entire range of sampled spatial frequencies. A simple functional form that fits our data is a broken power law $\hat{C}(f_\perp) \propto f_\perp^{-q}$ with $q = 2.32$ for $f < 0.062$ arcsec⁻¹ and $\hat{C}(f_\perp) \propto f_\perp^{-11/3}$, as expected for Kolmogorov turbulence, at higher frequencies. A power spectrum with a similar low-frequency slope and an abrupt high-frequency cut-off gives almost as good a fit to the observed structure functions, however. We can only determine an approximate lower limit to the outer scale: in terms of spatial frequency, $f_{\text{min}} \lesssim 0.005$ arcsec⁻¹ (0.015 kpc⁻¹). We conclude that these (and other, similar) models of the power spectrum cannot be distinguished using the available RM data alone. Our depolarization measurements at 1.5-arcsec resolution are also consistent with extrapolations of either power spectrum to higher spatial frequencies. In the South lobe of 3C 31, the model power spectra (normalized using the RM structure function) predict more depolarization than is observed at low resolution, however.

In Hydra A, we again fit the RM power spectrum with a power law, but measure a steeper slope, $q = 2.8$, than in 3C 31. We find no evidence for a high-frequency cut-off or for a portion of the power spectrum with the Kolmogorov slope at spatial frequencies $\lesssim 0.8$ kpc⁻¹ (cf. Vogt & Enßlin 2005).

RM analyses for sources in Abell clusters give qualitatively similar results. Murgia et al. (2004) found a spectral slope $q \approx 2$ extending to large spatial scales in Abell 119 and for Abell 2255, Govoni et al. (2006) argued for a spectral slope which steepens from $q \approx 2$ to $q \approx 4$ with increasing distance from the cluster centre. In contrast, Guidetti et al. (2008) found that a power-law power spectrum with a Kolmogorov slope and an abrupt long-wavelength cut-off at $f_{\text{min}} = 0.014$ kpc⁻¹ gave a very good fit to their RM and depolarization data for A2382, although a shallower slope $q \approx 2$ extending to longer wavelengths was not ruled out. All three of these studies assumed high-frequency cut-offs $f_{\text{max}} \approx 0.1$ kpc⁻¹.

In all cases except Hydra A (where the range of spatial scales we have investigated is very small), there is evidence

for a change in the power-law slope of the power spectrum, but ambiguity about its precise form. Two simple forms of the power spectrum which fit all of the datasets are:

(i) a broken power-law with a high-frequency slope $q_{\text{high}} = 11/3$ (the Kolmogorov value) and no high-frequency cut-off, but flattening to a slope $q_{\text{low}} \approx 2 - 3$ or even cutting off below a frequency $f_b \sim 0.01 - 1 \text{ kpc}^{-1}$ and

(ii) a power-law with index $q \approx 2 - 3$ extending to very low frequencies and a high-frequency cut-off at $f_{\text{max}} \sim 0.1 - 2 \text{ kpc}^{-1}$.

Other qualitatively similar models would also fit the data. Numerical simulations predict a wide range of spectral slopes (Dolag 2006), and a detailed comparison between theory and observation seems premature.

Our observation of a change in RM fluctuation amplitude across the nucleus of 3C 31 qualitatively supports the relativistic-jet interpretation of the brightness asymmetry between the jets, wherein the fainter (receding) jet is observed through a greater path length of magnetoionic medium than the nearer (approaching) jet. To test this idea quantitatively, we have modelled the global RM variations using three-dimensional simulations, again treating the magnetic field as an isotropic Gaussian variable with a broken power law power spectrum. We assume that the entire structure of 3C 31 has an inclination of 52° as in our kinematic models of the inner jets. The profile of the RM variance as a function of distance from the nucleus of the galaxy is incompatible with a spherically symmetric distribution for the magnetoionic medium as derived from X-ray observations: this would cause too gradual a variation. We expect, however, that the radio source will have evacuated cavities in the surrounding hot gas. A model in which the edges of the cavities coincide with the boundaries of the radio emission on large scales is more compatible with the observed RM profile, but current X-ray images are not deep enough to reveal any cavities around 3C 31. The derived central rms magnetic-field strength $B_0 \approx 0.7 \text{ nT}$ ($7 \mu\text{G}$) and the field varies roughly linearly with density. The magnetic field is not dynamically dominant over the volumes we model. The ratio of thermal to magnetic pressure, $\beta_P = p_{\text{thermal}}/(B^2/2\mu_0) \approx 10$ at the core radius of the group gas, $r_c = 154 \text{ arcsec}$ (52 kpc).

We have also modelled the RM distribution in Hydra A, where cavities *are* seen in X-ray images. A three-dimensional simulation including the cavities gives a good representation of the RM fluctuation profile for an inclination of $45 \pm 7 \text{ deg}$ with $B \propto n^{0.25 \pm 0.2}$ and a central magnetic field strength of 1.9 nT ($19 \mu\text{G}$), so $\beta_P \approx 30$ at $r_c = 26 \text{ arcsec}$ (27.7 kpc).

Close to the nuclei of both sources, our models predict higher RM fluctuation amplitudes than are observed. Although the sampling variances are large, this may be an indication that our assumption of a power-law dependence of magnetic field strength on density is oversimplified and that we have therefore overestimated the field strengths over these volumes.

Few other RM profiles have been published for FRI sources with jets, and it is not yet clear whether the abrupt changes in RM fluctuation amplitude across the nucleus observed in 3C 31 and Hydra A are common. In 3C 296 (Laing et al. 2006b), there is a smooth variation of rms RM across the nucleus, consistent with the inferred inclination

of 58° and Faraday rotation produced by a spherically symmetric hot gas component with a large core radius, as observed using *XMM-Newton* (Croston et al. 2008). The RM fluctuations observed in NGC 315 (Laing et al. 2006a) are too small to determine a reliable profile, although clearly larger on the counter-jet side.

7.2 Further work

Our modelling of the RM variations in 3C 31 and Hydra A suggests a number of observational and theoretical investigations.

(i) It is clearly necessary to sample a larger range of spatial scales to improve constraints on the RM power spectrum and in particular to decide whether it has the form expected for Kolmogorov turbulence on small scales. Higher *resolution* would probe small scales directly and remove the need to rely on crude estimates from depolarization. Higher *sensitivity* would provide better sampling of large spatial scales by allowing study of low-surface-brightness regions. Use of analysis techniques such as Bayesian maximum likelihood would give more rigorous error estimates. We have shown (Fig. 2b and c) that it is possible to derive accurate RM images from a small number of discrete frequencies in a suitably chosen observing band: the new generation of wideband correlators used by EVLA and eMERLIN will enable simultaneous observations over much larger frequency ranges, greatly improving the speed and accuracy of RM determination.

(ii) Large changes in RM fluctuation amplitude are seen across the nuclei in 3C 31 and Hydra A, but not in 3C 296. The prevalence of this phenomenon and its dependence on orientation, large-scale radio structure and environment are unknown. It is clear that the RM fluctuation amplitude scales with density, ranging from a few rad m^{-2} in sparse environments (e.g. NGC 315) to $\sim 10^4 \text{ rad m}^{-2}$ in cooling cores such as Hydra A. Observations of a larger sample, employing resolutions and frequency ranges matched carefully to the environments, will be needed.

(iii) We have argued that the presence of cavities in the external medium must be taken into account when modelling RM distributions: failure to do so will lead to biased estimates of the magnetic field strength and its variation with density. Accurate modelling requires knowledge of the source geometry (which we can constrain for 3C 31 but not Hydra A) and observations of the cavity structure (which are available for Hydra A but not yet for 3C 31). Deep *XMM-Newton* observations of the 3C 31 group are needed, as are comparable data for further sources. Kinematic models of the radio jets in Hydra A in other sources could be used to constrain their orientations.

(iv) Deviations in source structure and density from axisymmetry, Faraday rotation from foreground galaxies, X-ray emission from other group members in the field and from relativistic electrons deposited in the cavity by the radio source (via the inverse Compton process) and variations in the Galactic magnetic field across the source structure are potential complications which need to be better understood.

(v) The assumption that the magnetic field is an isotropic, Gaussian random variable is questionable. RM images of some radio sources show evidence for preferred di-

rections and there are theoretical reasons to suppose that fields at the edges of cavities and behind radio-source bow shocks should be two-dimensional. More detailed simulations of radio-source evolution in a magnetised intergalactic medium are needed.

ACKNOWLEDGEMENTS

RAL would like to thank the Istituto di Radioastronomia, NRAO and Alan and Mary Bridle for hospitality during the course of this work. We also thank Greg Taylor for allowing us to use his AIPS software for the analysis of rotation measure and for the images of Hydra A. Klaus Dolag, Torsten Enßlin and Corina Vogt kindly provided the PACERMAN RM images of 3C31 and Hydra A. We are particularly grateful to the referee, John Wardle, whose comments led to significant improvements in the paper, especially in the error analysis. We acknowledge travel support from NATO Grant CRG931498. The National Radio Astronomy Observatory is a facility of the National Science Foundation operated under cooperative agreement by Associated Universities, Inc.

REFERENCES

- Andernach, H., Feretti, L., Giovannini, G., Klein, U., Rossetti, E., Schnaubelt, J., 1992, *A&AS*, 93, 331
- Arp, H., 1966, *ApJS*, 14, 1
- Bicknell, G.V., Cameron, R.A., Gingold, R.A., 1990, *ApJ*, 357, 373
- Birzan, L., McNamara, B.R., Nulsen, P.E.J., Carilli, C.L., Wise, M.W., 2008, *ApJ*, in press, arXiv:0806.1929 (astro-ph)
- Bracewell, R., 2000, *The Fourier Transform and its Applications*, McGraw Hill, New York
- Burch, S.F., 1979, *MNRAS*, 187, 187
- Burn, B.J., 1966, *MNRAS*, 133, 67
- Carilli, C.L., Taylor, G.B., 2002, *ARAA*, 40, 319
- Croston, J.H., Hardcastle, M.J., Birkinshaw, M., Worrall, D.M., Laing, R.A., 2008, *MNRAS*, 386, 1709
- David, L.P., Nulsen, P.E.J., McNamara, B.R., Forman, W., Jones, C., Ponman, T., Robertson, B., Wise, M., 2001, *ApJ*, 557, 546
- De Vaucouleurs, G., De Vaucouleurs, A., Corwin, H.G. Jr., Buta, R., Paturel, G., Fouque, P., *Third Reference Catalogue of Bright Galaxies*, Springer-Verlag, New York
- Dineen P., Coles P., 2005, *MNRAS*, 362, 403
- Dolag, K., 2006, *AN*, 327, 575
- Dolag, K., Schindler, S., Govoni, F., Feretti, L., 2001, *A&A*, 378, 777
- Dolag, K., Vogt, C. Enßlin, T.A., 2005, *MNRAS*, 358, 726
- Dreher, J.W., Carilli, C.L., Perley, R.A., 1987, *ApJ*, 316, 611
- Dursi, L.J., Pfrommer, C., 2008, *ApJ*, 677, 993
- Eilek, J.A., Owen, F.N., 2002, *ApJ*, 567, 202
- Enßlin, T.A., Vogt, C., 2003, *A&A*, 401, 835
- Enßlin, T.A., Vogt, C., 2006, *A&A*, 453, 447
- Fabian, A.C., Sanders, J.S., Taylor, G.B., Allen, S.W., Crawford, C.S., Johnstone, R.M., Iwasawa, K., 2006, *MNRAS*, 366, 417
- Fanaroff, B.L., Riley, J.M., 1974, *MNRAS*, 167, 31P
- Felten J.E., 1996, in Trimble V., Reisenegger A., eds, *ASP Conf. Ser. 88, Clusters, Lensing and the future of the Universe*, Astron. Soc. Pac., San Francisco, p. 271
- Feretti, L., Perley, R., Giovannini, G., Andernach, H., 1999b, *A&A*, 341, 29
- Garrington, S.T., Conway, R.G., 1991, *MNRAS*, 250, 198
- Gizani, N.A.B., Leahy, J.P., 1999, *NewAR*, 43, 639
- Goldreich, P., Sridhar, S., 1997, *ApJ*, 485, 680
- Gopal-Krishna, Nath, B. B., 1997, *A&A*, 326, 45
- Gopal-Krishna, Wiita, P.J., 2000, *ApJ*, 529, 189
- Govoni F., Murgia M., Feretti L., Giovannini G., Dolag K., Taylor G.B., 2006, *A&A*, 460, 425
- Gradshteyn, I.S., Ryzhik, I.M., 1994, *Tables of integrals, series and products*, 5th ed., Academic Press, London
- Guidetti, D., Murgia, M., Govoni, F., Parma, P., Gregorini, L., de Ruiter, H.R., Cameron, R.A., Fanti, R., 2007, *A&A*, 483, 699
- Hardcastle, M.J., Worrall, D.M., Birkinshaw, M., Laing, R.A., Bridle, A.H., 2002, *MNRAS*, 334, 182
- Huchra, J.P., Vogeley, M.S., Geller, M.J., 1999, *ApJS*, 121, 287
- Kolmogorov, A.N., 1941, *Dokl. Nauk. Acad. SSSR*, 30, 301
- Komossa, S., Böhringer, H., 1999, *A&A*, 344, 755
- Kraft, R.P., Hardcastle, M.J., Worrall, D.M., Murray, S.S., 2005, *ApJ*, 622, 149
- Laing, R.A., 1988, *Nature*, 331, 149
- Laing, R.A., Bridle, A.H., 1987, *MNRAS*, 228, 557
- Laing, R.A., Bridle, A.H., 2002a, *MNRAS*, 336, 328
- Laing, R.A., Bridle, A.H., 2002b, *MNRAS*, 336, 1161
- Laing, R.A., Bridle, A.H., Canvin, J.R., 2006, *AN*, 327, 523
- Laing, R.A., Bridle, A.H., Parma, P., Feretti, L., Giovannini, G., Murgia, M. and Perley, R.A., 2008, *MNRAS*, 386, 657
- Laing, R.A., Canvin, J.R., Cotton, W.D., Bridle, A.H., 2006a, *MNRAS*, 368, 48
- Laing, R.A., Canvin, J.R., Bridle, A.H., Hardcastle, M.J., 2006b, *MNRAS*, 372, 510
- Leahy, J.P., 1987, *MNRAS*, 226, 433
- Martel, A., Baum, S. A., Sparks, W. B., Wyckoff, E., Biretta, J. A., Golombek, D., Macchetto, F. D., de Koff, S., McCarthy, P. J., Miley, G. K., 1999, *ApJS*, 122, 81
- Okuda, T., Kohno, K., Iguchi, S., Nakanishi, K., 2005, *ApJ*, 620, 673
- McNamara, B.R., Wise, M., Nulsen, P.E.J., David, L.P., Sarazin, C.L., Bautz, M., Markevitch, M., Vikhlinin, A., Forman, W.R., Jones, C., Harris, D.E., 2000, *ApJ*, 534, L135
- McNamara, B.R., Nulsen, P.E.J., 2007, *ARAA*, 45, 117
- Minter, A.H., Spangler, S.R., 1996, *ApJ*, 458, 194
- Morganti, R., Parma, P., Capetti, A., Fanti, R., de Ruiter, H.R., 1997, *A&A*, 326, 919
- Murgia, M., Govoni, F., Feretti, L., Giovannini, G., Dallacasa, D., Fanti, R., Taylor, G.B., Dolag, K., 2004, *A&A*, 424, 429
- Noel-Storr, J., Baum, S.A., Verdoes Kleijn, G., van der Marel, R.P., O’Dea, C.P., de Zeeuw, P.T., Carollo, C.M., 2003, *ApJS*, 148, 419
- Owen, F.N., Eilek, J.A., Keel, W.C., 1990, *ApJ*, 362, 449
- Owen, F.N., O’Dea, C.P., Keel, W.C., 1990, *ApJ*, 352, 44
- Perley, R.A., Bridle, A.H., Willis, A.G., 1984, *ApJS*, 54, 291
- Rudnick, L., Blundell, K.M., 2003, *ApJ*, 588, 143

- Schekochihin, A.A., Cowley, S.C., 2006, *Phys. Plasmas*, 13, 56501
- Scheuer, P.A.G., 1974, *MNRAS*, 166, 513
- Simonetti, J.H., Cordes, J.M., Spangler, S.R., 1984, *ApJ*, 284, 126
- Smith, R.J., Lucey, J.R., Hudson, M.J., Schlegel, D.J., Davies, R.L., 2000, *MNRAS*, 313, 469
- Smith, R.J., et al., 2004, *AJ*, 128, 1558
- Strom, R.G., Fanti, R., Parma, P., Ekers, R.D., 1983, *A&A*, 122, 305
- Tatarskii, V.I., 1971, *The effects of the turbulent atmosphere on wave propagation*, National Technical Information Service, US Department of Commerce, Springfield, VA
- Taylor, G.B., Perley, R.A., Inoue, M., Kato, T., Tabara, H., Aizu, K., 1990, *ApJ*, 360, 41
- Taylor, G.B., Perley, R.A., 1993, *ApJ*, 416, 554
- Tribble, P.C., 1991a, *MNRAS*, 250, 726
- Tribble, P.C., 1991b, *MNRAS*, 253, 147
- Tribble, P.C., 1992, *MNRAS*, 256, 281
- Vogt, C., Dolag, K., Enßlin, T.A., 2005, *MNRAS*, 358, 732
- Vogt, C., Enßlin, T.A., 2003, *A&A*, 412, 373
- Vogt, C., Enßlin, T.A., 2005, *A&A*, 434, 67
- Wise, M.W., McNamara, B.R., Nulsen, P.E.J., Houck, J.C. and David, L.P., 2007. *ApJ*, 659, 1153
- Zwicky, F., Kowal. C. T., 1968, *Catalogue of Galaxies and Clusters of Galaxies*, Vol.6, California Institute of Technology, Pasadena

APPENDIX A: NOTATION AND BASIC THEORY

In this Appendix, we summarise the basic theory of RM fluctuations in a foreground screen as given in the literature (Tribble 1991a; Enßlin & Vogt 2003; Murgia et al. 2004), primarily to establish notation and conventions for comparison with other work.

A1 Rotation measure

The rotation $\Delta\chi$ of the \mathbf{E} -vector position angle of linearly-polarized radiation by a foreground magnetized thermal plasma is given by:

$$\Delta\chi = K\lambda^2 \int nB_z dz = RM\lambda^2 \quad (\text{A1})$$

where n is the thermal electron density, B_z is the magnetic field component along the line of sight, RM is the rotation measure and

$$K = \frac{e^3}{8\pi^2 m_e^2 c^3 \epsilon_0} \quad (\text{A2})$$

in SI units. Alternatively,

$$\begin{aligned} \Delta\chi/\text{rad} &= 8.1193 \times 10^{-3} \\ &\times (\lambda/\text{m})^2 \int (n/\text{m}^{-3})(B_z/\text{nT})d(z/\text{kpc}) \end{aligned} \quad (\text{A3})$$

A2 Theory: real space

In what follows, we make the simplifying assumptions of Section 3.2: Faraday rotation is due entirely to a foreground medium in which the magnetic field is a Gaussian isotropic random variable and whose density and path length are uniform over the area of interest.

Our notation is similar to that of Enßlin & Vogt (2003). $\mathbf{r} = (x, y, z)$ is a vector of magnitude r with z along the line of sight and $\mathbf{r}_\perp = (x, y)$ (magnitude r_\perp) is a vector in the plane of the sky.

The magnetic autocorrelation function $w(r)$ and the RM autocorrelation function $C(r_\perp)$ are defined by:

$$\begin{aligned} w(r) &= \langle \mathbf{B}(\bar{\mathbf{r}}) \cdot \mathbf{B}(\bar{\mathbf{r}} + \mathbf{r}) \rangle \\ C(r_\perp) &= \langle \text{RM}(\mathbf{r}_\perp + \mathbf{r}'_\perp) \text{RM}(\mathbf{r}'_\perp) \rangle \end{aligned}$$

and are related by:

$$C(r_\perp) = K^2 n^2 L \int_{r_\perp}^{\infty} dr w(r) r (r^2 - r_\perp^2)^{-1/2}$$

The autocorrelation lengths for the magnetic field (λ_B) and RM (λ_{RM}) are of interest for comparison with other work. We adopt the definitions:

$$\lambda_B = \int_0^{\infty} dr \frac{w(r)}{w(0)} \quad (\text{A4})$$

$$\lambda_{\text{RM}} = \int_0^{\infty} dr_\perp \frac{C(r_\perp)}{C(0)} \quad (\text{A5})$$

These are equivalent to the expression given by Murgia et al.

(2004). The values given by Enßlin & Vogt (2003) are a factor of 2 larger.⁷ We also note that the mean square field $\langle B^2 \rangle = w(0)$ and that the average magnetic energy density $\langle \epsilon_B \rangle = w(0)/2\mu_0$ in SI units.

A3 Theory: Fourier space

Here, $\mathbf{f} = (f_x^2 + f_y^2 + f_z^2)^{1/2}$ (magnitude f) is a vector in frequency space with the f_z coordinate along the line of sight. $\mathbf{f}_\perp = (f_x, f_y)$ (magnitude f_\perp) is a frequency vector in the sky plane. We use the Fourier transform convention of Bracewell (2000), so for one dimension, spatial coordinate x and frequency f_x the transform pair $g(x)$ and $\hat{g}(f_x)$ are related by:

$$\begin{aligned}\hat{g}(f_x) &= \int_{-\infty}^{\infty} g(x) \exp(-2\pi i f_x x) dx \\ g(x) &= \int_{-\infty}^{\infty} \hat{g}(f_x) \exp(2\pi i f_x x) df_x\end{aligned}$$

In the isotropic case, we can define the two-dimensional RM power spectrum $\hat{C}(f_\perp)$ such that $\hat{C}(f_\perp)df_xdf_y$ is the power for an element df_xdf_y in frequency space. The RM power spectrum and autocorrelation function then form a Hankel transform pair [equation (6)]. We define the three-dimensional magnetic power spectrum $\hat{w}(f)$ such that $\hat{w}(f)df_xdf_ydf_z$ is the power in a volume $df_xdf_ydf_z$ of frequency space. This is the Fourier transform of the magnetic autocorrelation function and is very simply related to the RM power spectrum:

$$\hat{w}(f_\perp) = \frac{2\hat{C}(f_\perp)}{K^2 n^2 L} \quad (\text{A6})$$

For our model power spectra, it is most straightforward to evaluate autocorrelation lengths from integrals over $\hat{w}(f)$:

$$\lambda_B = \frac{1}{4} \frac{\int_0^\infty \hat{w}(f) f df}{\int_0^\infty \hat{w}(f) f^2 df} \quad (\text{A7})$$

$$\lambda_{\text{RM}} = \frac{1}{2\pi} \frac{\int_0^\infty \hat{w}(f) df}{\int_0^\infty \hat{w}(f) f df} \quad (\text{A8})$$

The constants in equations (A7) and (A8) differ by a factor of 4π from those in the equivalent expressions in Enßlin & Vogt (2003, their equation 39). 2π of this is because we use spatial frequency f rather than wavenumber k ($k = 2\pi f$) and the remaining factor of 2 is due to the definition of autocorrelation length, as explained above.

APPENDIX B: ANALYTICAL FORMULAE FOR STRUCTURE FUNCTIONS

B1 Power-law power spectrum

In order to validate our numerical approach to calculation of autocorrelation functions, we first consider a power spec-

trum which has a power-law form $\hat{C}(f_\perp) = f_\perp^{-q}$ for all frequencies f_\perp . The structure function then has a simple analytical form (Minter & Spangler 1996; Enßlin & Vogt 2003). In our notation and using equation (6):

$$\begin{aligned}C(r_\perp) &= 2\pi \int_0^\infty f_\perp^{1-q} J_0(2\pi f_\perp r_\perp) df_\perp \\ S(r_\perp) &= 2[C(r_\perp) - C(0)] \\ &= 4\pi \int_0^\infty f_\perp^{1-q} [1 - J_0(2\pi f_\perp r_\perp)] df_\perp \\ &= \frac{4\pi^{q-1} \Gamma(2 - q/2)}{q - 2} r_\perp^{q-2}\end{aligned} \quad (\text{B1})$$

for $2.5 < q < 4$.

For Gaussian convolution [equation (7)]:

$$\begin{aligned}C(r_\perp) &= 2\pi \int_0^\infty f_\perp^{1-q} J_0(2\pi f_\perp r_\perp) \exp(-2\pi\sigma^2 f_\perp^2) df_\perp \\ S(r_\perp) &= 4\pi \int_0^\infty f_\perp^{1-q} \exp(-2\sigma^2 f_\perp^2) [1 - J_0(2\pi f_\perp r_\perp)] df_\perp \\ &= \frac{2^{1+q/2} \pi^{q/2} \sigma^{q-2} \Gamma(2 - q/2)}{q - 2} \\ &\times \left[{}_1F_1 \left(1 - \frac{q}{2}, 1; \frac{-\pi r_\perp^2}{2\sigma^2} \right) - 1 \right]\end{aligned} \quad (\text{B2})$$

where we have integrated once by parts. We obtain three terms: two of these can be integrated using equation 6.631.1 of Gradshteyn & Ryzhik (1994) and combined with equation 9.212.2 from the same reference to give a single confluent hypergeometric function ${}_1F_1$ multiplied by a Γ function; the third is the integral representation of the same Γ function.

B2 The small-separation limit

Quite generally, the structure function for a power spectrum which is bounded in frequency (unlike the asymptotic case of equation B1) will be quadratic, $S(r_\perp) \propto r_\perp^2$ for sufficiently small separations r_\perp (Tatarskii 1971; Tribble 1991a). For a power spectrum $\hat{C}(f_\perp)$, the structure function is:

$$S(r_\perp) \approx 4\pi^3 r_\perp^2 \int_0^\infty \hat{C}(f_\perp) f_\perp^3 df_\perp$$

provided that $f_\perp r_\perp \ll 1$ over the full range of the integral. Similarly for a Gaussian convolving beam,

$$S(r_\perp) \approx 4\pi^3 r_\perp^2 \int_0^\infty \hat{C}(f_\perp) f_\perp^3 \exp(-2\pi\sigma^2 f_\perp^2) df_\perp$$

For the specific example of the cut-off power law spectrum of equation 9 without convolution,

$$S(r_\perp) \approx \frac{4\pi C_0 f_{\text{max}}^{4-q} r_\perp^2}{4 - q}$$

The structure function at small separations then has the same functional form as equation B1 for a power-law index of $q = 4$, leading to possible confusion between power spectra with high-frequency cut-offs and steep power laws extending to high frequencies.

⁷ Enßlin & Vogt (2003)'s definitions of autocorrelation lengths are problematic, as they integrate from $-\infty$ to $+\infty$ in r and r_\perp , both of which are intrinsically positive quantities.

APPENDIX C: ROTATION AND DEPOLARIZATION AT LONGER WAVELENGTHS

In this Appendix, we simulate the Faraday rotation and depolarization expected from our model RM power spectrum under conditions where the short-wavelength approximation does not hold, primarily to aid interpretation of other observations.

In Fig. C1, we show the results of a simulation using the method described in Section 4.5. The RM power spectrum has the BPL form with the parameters given in Table 1 and an amplitude, $D_0 = 0.38$, chosen to match the observed depolarization in region SP3. Fig. C1(a) shows the simulated RM image convolved to a resolution of 5.5 arcsec. The image calculated by evaluating Q and U on a fine grid, convolving them to 5.5 arcsec resolution, deriving the position angle χ and fitting for the RM is shown in Fig. C1(b). Although this is close to the convolved RM image in most locations, it also shows discrepant values associated with large RM gradients across the beam. These artefacts are extended perpendicular to the direction of maximum RM gradient and are always accompanied by strong depolarization, as shown in Fig. C1(c). We see a few artefacts of the predicted type in the observed 5.5 arcsec RM image, again associated with high RM gradients: two examples are shown in Fig. C2. The reason for the artefacts is that there are large deviations from λ^2 rotation, and the RM fitting algorithm does not correct properly for the $n\pi$ ambiguities in \mathbf{E} -vector position angle. This is illustrated in Fig. C3 by plots of χ against λ^2 at the points labelled a – d in Fig. C1 (these are ordered from least to most depolarized). At position a, the RM gradient is small and there is negligible deviation from λ^2 rotation. Positions b and c are intermediate cases: $\Delta\chi$ is not perfectly proportional to λ^2 , but the deviations are small enough for the RM fitting algorithm to find a reasonable approximation to the correct solution. Finally, position d is in a region of high RM gradient with large deviations from λ^2 rotation. The fitting algorithm then introduces spurious $n\pi$ corrections to the position angles and finds an incorrect RM, as is clear from Fig. C1(b). Such deviations from λ^2 rotation can occur even at points with high signal-to-noise ratio, and may not, therefore, be corrected even by fitting algorithms like PACERMAN (Dolag et al. 2005), which take account of the spatial coherence of RM.

For the range of RM, observing frequency and resolution appropriate to our observations of 3C 31, such artefacts do not pose a serious problem, however. Firstly, they should cover a small fraction of the area, even in SP3. Secondly, they inevitably have low polarized flux density at low frequency and are therefore usually excluded from RM fits on grounds of low signal-to-noise ratio.

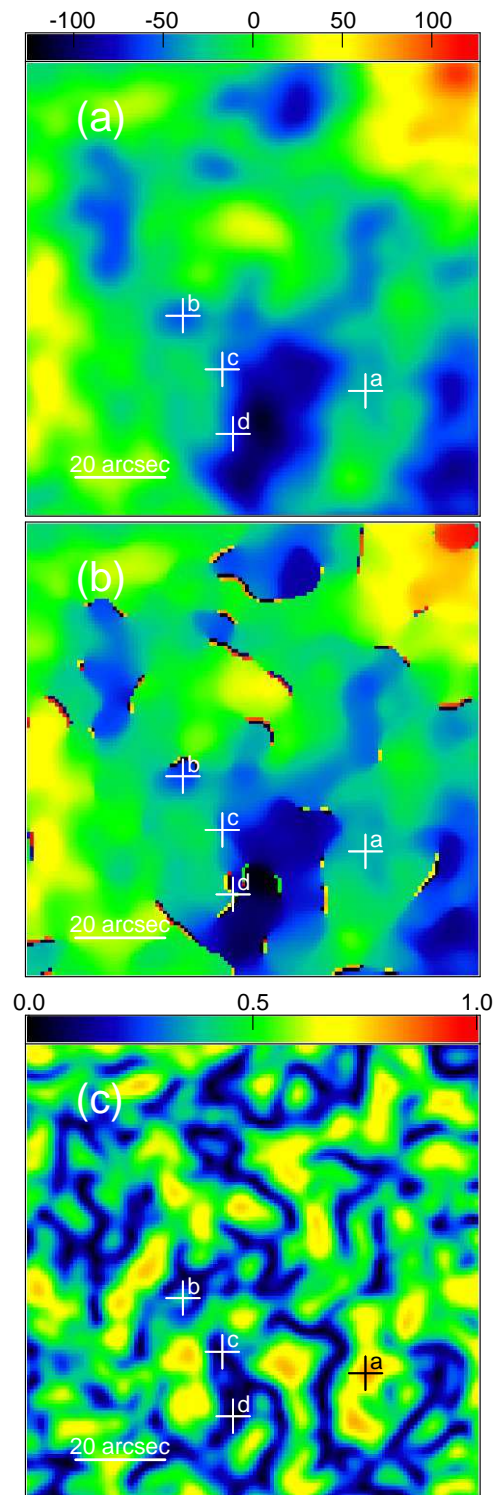


Figure C1. Simulated RM and p images generated from a realisation of the BPL power spectrum described in the text, computed on an 8192×8192 grid with 0.05 arcsec pixels. The amplitude is $D_0 = 0.38$ and the remaining parameters are as given in Table 1. The crosses show the locations for the $\chi - \lambda^2$ plots in Fig. C3. (a) Model RM image convolved with a 5.5-arcsec FWHM Gaussian. (b) Model RM image of the same area derived by generating Q and U images at 5 observing frequencies, convolving them to 5.5-arcsec resolution and fitting $\Delta\chi = RM\lambda^2$ as for the observations. (c) Ratio of the degree of polarization at 1365 MHz to the value at infinite frequency, derived from the convolved Q and U images.

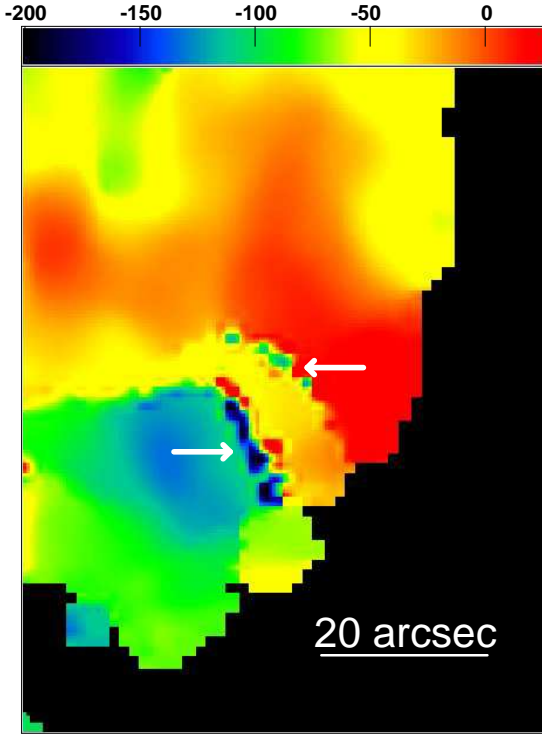


Figure C2. Part of the *observed* RM image of the South lobe of 3C 31 from Fig 2(c). Two examples of artefacts in regions of high RM gradient are indicated by white arrows.

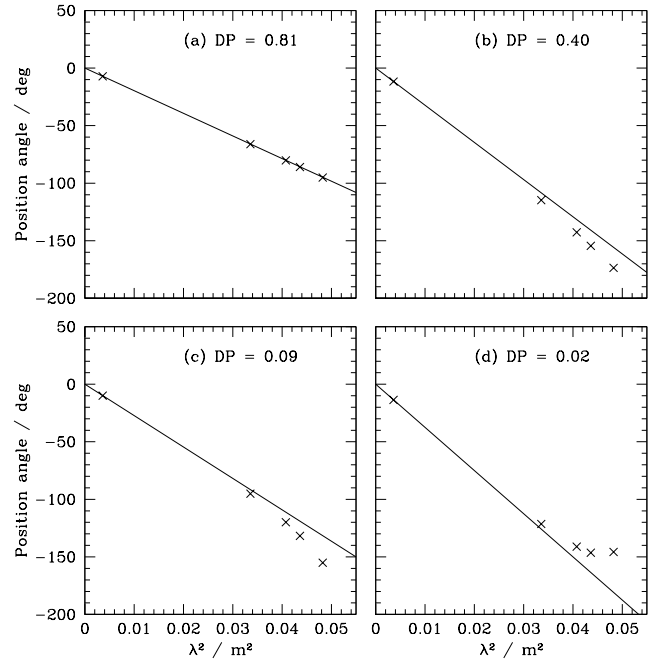


Figure C3. Plots of position angle against λ^2 for simulated data with the BPL RM power spectrum and an amplitude $D_0 = 0.38$, as required to match the depolarization in region SP3 of 3C 31. The corresponding RM and depolarization images are shown in Fig. C1, where the locations corresponding to individual panels are marked. The full lines correspond to the RM's from Fig. C1(a) and DP is the ratio of the polarization at 1365 MHz to its intrinsic value. The panels are arranged from least to most depolarized. Panel (a) has DP = 0.81 and shows accurate λ^2 rotation at the correct RM. Panels (b) – (d) correspond to positions with higher RM gradients, stronger depolarization ($DP \ll 1$) and significant deviations from λ^2 rotation. At position (d), the RM fitting algorithm has become confused, leading to the RM anomaly visible in Fig. C1(b).